CHALMERS
UNIVERSITY OF TECHNOLOGY

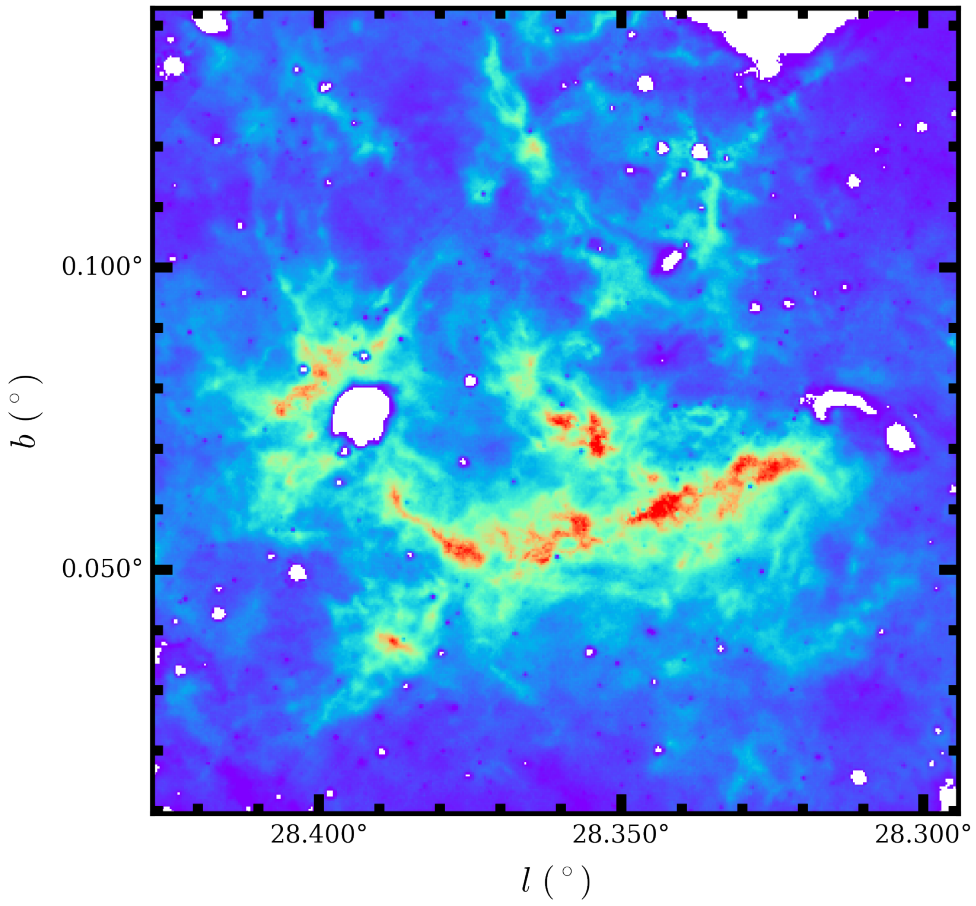

The Dynamical State of a Massive Infrared Dark Cloud Filament

Master's thesis in Physics

Carl Larsson

DEPARTMENT OF SPACE, EARTH AND ENVIRONMENT
CHALMERS UNIVERSITY OF TECHNOLOGY
Gothenburg, Sweden 2024
www.chalmers.se

Master's thesis 2024

The Dynamical State of a Massive Infrared Dark Cloud Filament

Carl Larsson

CHALMERS
UNIVERSITY OF TECHNOLOGY

Department of Space, Earth and Environment
Division of Astronomy and Plasma Physics
Chalmers University of Technology
Gothenburg, Sweden 2024

The Dynamical State of a Massive Infrared Dark Cloud Filament
Carl Larsson

Supervisor: Chi-Yan Law, Department of Space, Earth and Environment
Examiner: Prof. Jonathan Tan, Department of Space, Earth and Environment

Master's Thesis 2024
Department of Space, Earth and Environment
Division of Astronomy and Plasma Physics
Chalmers University of Technology
SE-412 96 Gothenburg
Telephone +46 31 772 1000

Cover: Spitzer mid infrared extinction map.

Typeset in LaTeX
Gothenburg, Sweden 2024

Abstract

Infrared dark clouds (IRDCs) are cold, dense regions seen as dark features against the galactic mid infrared (MIR) background, and are believed to be the progenitors of massive star and star cluster formation. It is thus of interest to characterize the dynamical state of IRDCs, since it provides important information to constrain the existing theoretical models of massive star and star cluster formation. Here, the virial state of the massive filamentary IRDC G28.37+0.07 is studied by deriving mass from a mass surface density map derived from far infrared (FIR) observations using the Herschel Space Observatory, and velocity dispersion from $C^{18}O(1-0)$ line emission observed with the Green Bank Telescope (GBT). In contrast to many previous studies, the support from magnetic pressure is also quantified based on a magnetic field strength map derived from SOFIA HAWC+ 214 μm polarized dust emission data. The virial state of G28.37+0.07 is found to vary along the main filament of the cloud,. The central part is found to be close to virial equilibrium, while the eastern and western ends are found not to be. As more continuum sources have been found towards this central region than the ends, this result might support the idea of massive stars forming in equilibrium conditions. The state of $C^{18}O$ depletion is also studied as part of this work. The depletion factor is found to be generally $f_D > 3$ towards the main part of the cloud, with certain regions showing values of the depletion factor upwards of 10. This suggests $C^{18}O$ is significantly depleted from the gas phase and frozen out onto dust grains. The overall findings of this study will provide further information towards understanding the details of the complex processes of massive star and star cluster formation.

Acknowledgements

I would like to thank Prof. Jonathan Tan for the opportunity of doing this work, as well as providing lots of useful feedback over the course of the project. I also want to thank my supervisor Dr. Chi-Yan Law for bearing with me through all of our meetings and answering all of my questions. This project would not have been the same without you! Last, but not least, I want to thank my friends and family, especially Alva, for all of their encouragement throughout the course of this project.

Carl Larsson, Gothenburg, June 2024

Contents

List of Figures **xi**

List of Tables **xv**

1 Introduction **1**
1.1 Massive star formation . . . 1
1.2 Interstellar filaments . . . 2
1.3 Infrared Dark Clouds . . . 2
1.3.1 IRDC G28.37+00.07 . . . 3
1.4 Aims and outline of the thesis . . . 4

2 Theory **5**
2.1 Filamentary virial analysis . . . 5
2.1.1 Virial theorem . . . 5
2.1.2 Fiege-Pudritz model of virial equilibrium . . . 6
2.1.3 Previous studies on filamentary virial analysis . . . 7
2.2 Radiative transfer . . . 8
2.3 Depletion . . . 10
2.3.1 Previous studies on CO depletion in IRDCs . . . 10

3 Data & Methods **11**
3.1 Data . . . 11
3.1.1 SOFIA-HAWC+ . . . 11
3.1.2 GBT-$C^{18}O$ data . . . 11
3.1.3 Archival extinction and mass surface density maps . . . 12
3.1.4 ALMA continuum and $C^{18}O$ data . . . 12
3.2 Offset analysis . . . 12
3.2.1 Linear structure offset estimation . . . 13
3.2.2 Offset estimation using radial profiles . . . 15
3.3 Filamentary virial analysis . . . 17
3.3.1 Filament geometry and envelope subtraction . . . 17
3.3.2 Relevant parameters . . . 20
3.4 Depletion analysis . . . 21

4 Results **23**
4.1 Filamentary virial analysis . . . 23
4.2 Depletion analysis . . . 31

5 Discussion & Conclusions **35**
5.1 The virial state of G28.37+0.07 35
5.2 $C^{18}O$ depletion 35
5.3 Conclusions and future outlooks 37

Bibliography **39**

A Additional table and figures **I**

List of Figures

3.1 Extracted spines for offset estimation from the extinction map (blue squares) and the GBT $C^{18}O$ integrated intensity map (cyan dots, map in background). Also shown is the 65 mag contour from the extinction map. 13

3.2 Histograms of the computed offsets between the spines extracted from the GBT $C^{18}O$ integrated intensity map and the extinction map (cyan dots and blue squares respectively in Figure 3.1). Top left: Offsets computed along the galactic longitude direction. Top right: Offsets computed along the galactic latitude direction. Bottom left: Minimum absolute offsets. Bottom right: Offsets computed in the direction perpendicular to the extinction spine. In the top right of each panel the median of the corresponding distribution can be found. . . 14

3.3 Top left: ALMA continuum image of peak 1 (seen in the center, and marked by the black plus in the other panels). Bottom left: GBT $C^{18}O$(1-0) integrated intensity. Top right: ALMA $C^{18}O$(2-1) integrated intensity (78.0−79.0 km/s). Bottom right: ALMA $C^{18}O$(2-1) integrated intensity regridded to match the spatial pixel scale of the GBT $C^{18}O$(1-0) emission. In all panels except the top left, a contour from the ALMA continuum image at 0.002 Jy/beam is overlaid. . . . 16

3.4 Top left: Herschel mass surface density map. Top right: GBT $C^{18}O$ integrated intensity map. Middle left: Spitzer MIR extinction map with positions of detected ALMA continuum sources marked as black plus signs. The larger the marker appears, the more massive the source was estimated to be. Overlaid as a drapery is the inferred plane of sky magnetic field component. Middle right: Velocity dispersion map from Law et al. (2024). Bottom left: Plane of sky magnetic field strength map. Bottom right: Map of the magnetic field component along the filament (i.e. in the east-west direction). In each panel, the inner and outer filament regions are overlaid as dashed white and solid red lines, respectively, as well as MIR extinction contours at A_V = 7, 15, 30, 60 mag. 18

3.5 Schematic view of a cross section of the filament and its envelope. . . 19

4.1 Spectra for the inner strip regions for strips 1-4 (bottom to top). The red solid lines in both panels are the spectra extracted from the "on" regions, and the green dashed lines show the respective zero-points for the different spectra. The left panel also shows the spectra from the north and south envelope regions (dashed blue and dot-dashed brown respectively). The right panel also shows the scaled average spectra of the envelope regions (dashed blue), and the envelope subtracted filament spectra (solid black). 24

4.2 Same as Figure 4.1, but for strips 5-8 (bottom to top). 24

4.3 Same as Figure 4.1, but for strips 9-11 (bottom to top). 25

4.4 Same as Figure 4.1, but for strips 12-14 (bottom to top). 25

4.5 Same as Figure 4.1, but for for the outer strip regions. 25

4.6 Same as Figure 4.5, but for strips 5-8 (bottom to top). 26

4.7 Same as Figure 4.5, but for strips 9-11 (bottom to top). 26

4.8 Same as Figure 4.5, but for strips 12-14 (bottom to top). 26

4.9 Comparison figures for the different cases of envelope subtraction for the filament line mass (m_f, left), virial line mass ($M_{\mathrm{vir},f}$, middle), and the ratio of the two (right). Top panels are for the inner filament case, while the bottom panels are for the outer filament case. The blue represents the no envelope subtraction case, the red is for masses envelope subtracted, and the black is for both masses and spectra envelope subtracted. 27

4.10 Comparison figures for the different cases of envelope subtraction for the filament pressure (P_f, left), envelope pressure (P_e, middle), and the ratio P_e/P_f (right). Top panels are for the inner filament case, while the bottom panels are for the outer filament case. The blue represents the no envelope subtraction case, the red is for masses envelope subtracted, and the black is for both masses and spectra envelope subtracted. 28

4.11 Ratio of envelope to filament pressure, P_e/P_f, against filament line mass ratio, $m_f/m_{\mathrm{vir},f}$. The top panel shows the case of no envelope subtraction. The middle panel shows the case where mass surface densities have been envelope subtracted. The bottom panel shows the case where mass surface densities and spectra have been envelope subtracted. The dashed and dotted lines correspond to different values of $\mathcal{M}/|\mathcal{W}|$ in Equation (2.5): The magnetically neutral case ($\mathcal{M}/|\mathcal{W}| = 0$, dashed), and magnetic confinement (< 0, dotted) and support (> 0, also dotted) (see top panel for exact values). The typical error of the quantities is also shown in the top left panel. . . 29

4.12 Comparisons of the left and right hand sides of Equation (2.6). The top row shows the case without envelope subtraction, the middle row the case with masses envelope subtracted, and the bottom row shows the case with masses and spectra envelope subtracted. The left column shows the case where the magnetic surface pressure has been neglected, while the right column considers it. The gray line is the virial (one-to-one) line. Red and blue points are for the inner and outer filament regions respectively. 30
4.13 Left: Observed $C^{18}O$ column density (i.e. computed from the $C^{18}O$ data). The data has been regridded to match the spatial resolution of the Herschel mass surface density map. Right: Expected $C^{18}O$ column density computed from the Herschel column density map. . . 32
4.14 Left: Observed $C^{18}O$ column density (i.e. computed from the $C^{18}O$ data). Right: Expected $C^{18}O$ column density computed from the Spitzer extinction map regridded to match the spatial resolution of the GBT $C^{18}O$(1-0) data. 32
4.15 Left: Depletion map derived from the Herschel mass surface density map and the GBT $C^{18}O$ data, assuming $T_{ex} = 7.5$ K. Right: Same as on the left, but assuming $T_{ex} = 20$ K towards the C9 region (marked by the black box in both panels). The color scale has been truncated at 10 to match the peak value of the depletion factor outside of the C9 region. 33
4.16 Depletion map derived from the Spitzer extinction map and the GBT $C^{18}O$ data, assuming $T_{ex} = 7.5$ K. 33

5.1 Ten regions studied by Entekhabi et al. (2022) (red circles) overlaid on the depletion map of the left panel of Figure 4.15. 36
5.2 Comparisons between the depletion factors derived in this work ($f_D(L)$) and those derived from the abundances of Entekhabi et al. (2022) ($f_D(E)$). The left panel has f_D(L) computed from the velocity range $70 - 85$ km/s, while in the right panel it is instead computed from the range $77 - 82$ km/s, matching the range used in Entekhabi et al. (2022). 36

A.1 As Figure 3.3, but for continuum peak 2, and with integration interval $77.5 - 78.5$ km/s. II
A.2 As Figure 3.3, but for continuum peak 3, and with integration interval $77.5 - 78.9$ km/s. III
A.3 As Figure 3.3, but for continuum peak 4, and with integration interval $78.6 - 79.2$ km/s. IV

List of Tables

3.1 Positions (galactic longitude and latitude) of some continuum (columns 2 and 3), ALMA $C^{18}O$(2-1) (columns 4 and 5), and GBT $C^{18}O$(1-0) (columns 6 and 7) emission peaks (column 1), as well as position angles and distances between the different peaks (continuum-$C^{18}O$(2-1) in columns 8 and 9, and $C^{18}O$(2-1)-$C^{18}O$(1-0) in columns 10 and 11). 16

A.1 Values for the different quantities. The first row for each quantity is without envelope subtraction, while second and third rows show envelope subtracted quantities (Without brackets: only Σ subtracted. With brackets: spectra also subtracted.). For the magnetic energies per unit length, the first and second rows are without and with the surface term respectively. The last column shows a total (either sum or mean) of the 14 strips. I

1

Introduction

Stars in general, and massive stars (with masses greater than $8M_{\odot}$) in particular, are a large driving force in the evolution of galaxies. During their lifetime they radiate huge amounts of energy, as well as injecting turbulence into the interstellar medium (ISM) through jets and stellar winds, among other things. Due to the fusion processes inside their cores, the material ejected from the stars will be enriched with heavy elements. In the case of low- and intermediate-mass, they mainly inject helium, carbon and nitrogen into the surrounding medium, while massive stars also produce even heavier elements (Lamers & Levesque, 2017). While the formation mechanisms of low mass stars are thought to be generally well understood, the same cannot be said for the high-mass case. Despite their importance, there are several open questions remaining regarding how massive stars form, such as: Is there a simple model to explain high-mass star formation? And which processes regulate high-mass star formation.

1.1 Massive star formation

There are currently two main theories of massive star formation: 1) Core accretion (e.g. the turbulent core accretion (TCA) model of McKee & Tan, 2003) and 2) Competitive accretion (e.g. Bonnell et al., 1997, 2001). The former is essentially a scaled up version of low-mass star formation (Shu et al., 1987). In this scenario, the initial conditions are self-gravitating cores of gas that condense from a larger fragmenting clump (see e.g. Tan et al., 2014). These cores then undergo gravitational collapse to form a single star or a small-N multiple stellar system. In contrast to low-mass star formation, where the internal pressure of the cores consists of mainly thermal pressure, in high-mass star formation turbulence and/or magnetic fields are thought to dominate. In the case of the fiducial TCA model, near equipartition of turbulence and magnetic fields is assumed. On the other hand, in the scenario of competitive accretion stars gain their mass more chaotically from a wide region of the clump. For this scenario, massive, gravitationally bound, starless cores are not required to form massive stars Tan et al. (2014). This results in the formation of stellar clusters, with the most massive stars forming in the cluster centers, since that will be the deepest part of the gravitational potential well (Bonnell et al., 1997, 2001). Further, if the density of protostars becomes sufficiently high in the cluster center, stellar collisions may play a role in forming the most massive stars.

In both of these scenarios, several different mechanisms are thought to regulate the formation process of massive stars. Self gravity, turbulence and magnetic fields

are some among these processes. However, the relative importance of magnetic fields compared to the others still is not well understood (Pattle et al., 2023). It is thus of importance to study magnetic fields to further the understanding of the processes that regulate massive star formation.

1.2 Interstellar filaments

Interstellar filaments are structures with large aspect ratios (length/width). Such structures have been known to exist for quite some time. For instance, Schneider & Elmegreen (1979) reported a catalog of 23 globular filaments, which they stated to be filamentary dark clouds with clear condensations into smaller, discrete so called globules. A later study by McClure-Griffiths et al. (2006) found a network of filaments in the Riegel-Crutcher HI cloud. Some of their detected filaments were found to have aspect ratios upwards of 170, stemming from lengths of ~ 17 pc. McClure-Griffiths et al. (2006) also state that comparisons between the HI images and the observed polarization indicates that the filaments are aligned with the ambient magnetic field, indicating that magnetic fields might be important in the formation of filaments. Furthermore, Falgarone et al. (2001) report the observation of several filaments, traced by ^{12}CO, converging on a dense core. Thus, filaments have been observed across several different environments, and traced by different mechanisms.

However, the area of filament research was revolutionized by the launch of the Herschel Space Observatory in May 2009. Due to its high sensitivity, it was able to detect filamentary structures across a wide range of scales, and with higher resolution, than previously possible from ground (André et al., 2014). Regardless of star formation content, every cloud observed with Herschel showed filamentary structure. Thus, the formation of filaments seems to happen before stars begin to form. Furthermore, results from the Herschel Gould Belt Survey (HGBS, a survey of nearby clouds) find that over 70% of prestellar cores found with Herschel have been detected in filaments (André et al., 2014). This connection between filaments and cores suggests that filaments play a role in the initial stages of the star formation process.

Filamentary structures have since been observed over a wide range of scales, and within many different environments. From the largest kpc scale objects connected to spiral arms, to sub-pc scale structures within individual clouds, as well as from the atomic interstellar medium to the very dense regions harboring massive star formation (Hacar et al., 2023).There have also been observations showing connections between filament networks and massive star formation, as well as IRDCs, using the Atacama Large Millimeter Array. This further emphasizes the importance of studying filaments to better understand the formation mechanisms of stars.

1.3 Infrared Dark Clouds

Infrared Dark Clouds (IRDCs) is one of the most massive classes of molecular clouds, and Rathborne et al. (2006) found masses on the order of $10^2 - 10^4$ $M_\odot$ within their selected sample of 38 clouds. As the name suggests, they appear as dark features

against the galactic mid-infrared background, and they are often identified as such absorption features in images from the Spitzer/GLIMPSE survey (Hacar et al., 2023). IRDCs are also cold ($T \sim 10-20$ K) and dense (10^2-10^4 cm^{-3}) (as reported for the sample of Rathborne et al., 2006). IRDCs have also been observed to come in several different shapes. Some are compact, while others show filamentary structure in parts or overall (Rathborne et al., 2006; Hacar et al., 2023). Hence, IRDCs can be great candidates for studying massive star formation, since their properties match that of thought to be early stage massive star forming cores, as well as the filaments having been seen to harbor many cores (see Section 1.2).

The initial stages of low-mass star formation are thought to be generally well understood. The earliest stage in this process are the so called Bok globules, within which pre-protostellar cores are found (Rathborne et al., 2006). These cores are then thought to collapse under their own gravity, and eventually form stars. The high-mass counterpart, however, is less well understood. Rathborne et al. (2006) state that the earliest stage of massive star formation known at the time is the so called "hot cores". These hot cores are characterized by being more massive and dense, and with higher temperatures ($T \sim 50-250$ K), than the low-mass pre-protostellar cores. However, these hot cores represent an evolutionary stage where a protostar has already formed, and thus they cannot be the earliest stage of massive star formation. Rathborne et al. (2006) then proposes that there should be a high-mass analogue to Bok globules, and that this analogue could be IRDCs. They support this claim by stating that they detect cores within IRDCs with the same physical characteristics as hot cores, with the only significant difference being that these IRDC cores have lower temperatures. Thus, in order to constrain the initial condition of massive star formation, the physical conditions of IRDCs should be studied.

1.3.1 IRDC G28.37+00.07

In this work, the focus is on the IRDC G28.37+00.07, which will be referred to as Cloud C (Butler & Tan, 2009, 2012) throughout the remainder of this work. It was reported as dark lanes against the infrared background of the galaxy by Simon et al. (2006a), and lies at a distance of 5.0 kpc from the sun (Simon et al., 2006b). Since its discovery it has been studied extensively in many different aspects. One such aspect is mass surface density mapping, which has been performed using mid-infrared (MIR) extinction (MIREX) mapping (Butler & Tan, 2009, 2012; Butler et al., 2014) and graybody fits to sub-millimeter data (Lim et al., 2016). From such studies, the mass of Cloud C has been estimated to $\sim 7{\cdot}10^4\ M_\odot$, making it one of the most massive IRDCs known. Hernandez & Tan (2015) studied the gas kinematics of the cloud using ^{13}CO(1-0) emission, finding a central velocity around 78.5 km/s, matching what has been found previously (e.g. 78.6 km/s by Rathborne et al., 2006). There have also been studies on the fragmentation properties of Cloud C, with Moser et al. (2020) studying the population of young stellar objects (YSOs), Kong (2019) studying the core mass function (CMF), and Barnes et al. (2023) studying the detailed fragmentation of a single core. The cores have also been observed to have corresponding molecular outflows, and the directions of these have been studied

compared to the main filament orientation (Kong et al., 2019a) and to the magnetic field orientations (Law et al., 2024). Further, the large scale magnetic field properties have been studied by Law et al. (2024) and Liu et al. (2024). Yet another study of this cloud was done by Entekhabi et al. (2022), who studied the chemical properties towards ten locations within the cloud. They computed abundances towards these ten regions for a number of molecules, including $C^{18}O$, from observations using the Instituto de Radioastromía Milimétrica (IRAM) 30 m telescope. Missing from this list of properties is a proper assessment of the energetics and state of CO depletion, which are both investigated in this work. The energetics are also presented in a coming publication (Larsson et al. in prep).

1.4 Aims and outline of the thesis

The aim of this thesis is to investigate the dynamical state of the main filament structure of the IRDC G28.37+0.07. The aim is to investigate the relative importance of kinetic, gravitational, and magnetic pressures through a filamentary virial analysis. The state of $C^{18}O$ depletion across the cloud is also investigated.

The outline of this thesis is as follows. In Chapter 2, some relevant theory to the applied methods is presented. In Chapter 3, the methods of the analysis is presented. Chapter 4 presents the obtained results, including the virial state of the cloud and maps of the state of depletion. Finally in Chapter 5, the results of the virial analysis are put in the context of massive star formation, and the state of depletion is compared to previous studies. Some conclusions are also presented.

2

Theory

In this chapter aims to give the reader some theoretical background on the topics presented in this work. This includes an introduction to the virial theorem, and in particular the version applicable to filamentary structures. A brief description of radiative transfer and its use in astronomical calculations is presented, as well as an introduction to the concept of depletion. Some previous studies are also presented.

2.1 Filamentary virial analysis

In this section, the virial theorem is introduced, and derivations of the relevant equations relating to the filamentary case are given.

2.1.1 Virial theorem

The virial theorem states the relative importance of different forms of energy within a system. It can be derived by taking the second time derivative of the moment of inertia

$$I = \int \rho r^2 dV,$$

after which one gets

$$\frac{1}{2}\ddot{I} = 2E_{\mathrm{KE}} + 3\Pi + E_{\mathrm{mag}} + E_{\mathrm{grav}} - \oint \left(P + \frac{B^2}{8\pi}\right)\vec{x}\cdot d\vec{S} + \frac{1}{4\pi}\oint(\vec{x}\cdot\vec{B})\vec{B}\cdot d\vec{S} \quad (2.1)$$

(see Draine, 2011, for a proper derivation). The four first terms are the kinetic energy due to large scale motion within the cloud, the pressure integral, the magnetic energy, and the gravitational potential energy respectively. These can be computed as

$$E_{\mathrm{EK}} = \int \frac{\rho v^2}{2} dV,$$

$$\Pi = \int P dV,$$

$$E_{\mathrm{mag}} = \int \frac{B^2}{8\pi} dV,$$

and

$$E_{\mathrm{grav}} = -\int \vec{x}\cdot\nabla\Phi dV.$$

Krumholz (2015) gives an interpretation of the different cases for the sign of $\ddot{I}$: If it is negative, gravity, surface pressure and magnetic pressure and tension at the surface

dominate, and the gas accelerates inward. If it is positive, the thermal pressure, ram pressure, and magnetic pressure dominate, and the gas accelerates outward. If it instead is zero, the rate of collapse/expansion remains constant. The virial theorem is usually applied to systems in steady state, that is with $\ddot{I} = 0$.

2.1.2 Fiege-Pudritz model of virial equilibrium

Fiege & Pudritz (2000) modeled magnetized, filamentary clouds as cylinders threaded by general helical magnetic fields. They derived a more useful form of the filamentary virial equation, starting from

$$K + M + W = 0, \tag{2.2}$$

where K is the internal energy due to both thermal and non-thermal motions, M is the magnetic energy, and W is the gravitational potential energy. These energies are given by

$$K = 3\int_V P dV - \oint P\vec{x} \cdot d\vec{S},$$

$$M = \frac{1}{8\pi}\int_V B^2 dV + \frac{1}{4\pi}\oint (\vec{x}\cdot\vec{B})(\vec{B}\cdot d\vec{S}) - \frac{1}{8\pi}\oint B^2\vec{x}\cdot d\vec{S},$$

and

$$W = -\int_V \rho\vec{x}\cdot\nabla\Phi dV.$$

Here P is kinetic pressure, B is the magnetic field strength, and ρ is the mass density. The different integrals in these expressions can be evaluated. By considering the cylindrical geometry and constant values for the pressure and B-field components on the radial surface of the cylinder we then end up with

$$0 = 2\int P d\mathcal{V} - 2P_S\mathcal{V} + \mathcal{W} + \mathcal{M} \tag{2.3}$$

(see Fiege & Pudritz, 2000, for details). Here $\mathcal{V}$ is the volume per unit length (or cross sectional area) of the filament, $\mathcal{W}$ is the gravitational energy per unit length given by

$$\mathcal{W} = -\int \rho r\frac{\partial\Phi}{\partial r} d\mathcal{V} = ... = -m^2 G, \tag{2.4}$$

m being the mass per unit length, and G being the gravitational constant, and $\mathcal{M}$ is the magnetic energy per unit length given by

$$\mathcal{M} = \frac{1}{4\pi}\int B_z^2 d\mathcal{V} - \frac{B_{z,S}^2 + B_{\phi,S}^2}{4\pi}\mathcal{V},$$

where a subscript S indicates that the quantity is evaluated at the radial surface of the filament (again see Fiege & Pudritz, 2000, for details).

From Equation (2.3) it is now possible to derive a useful form of the virial equation. As in Fiege & Pudritz (2000), we define the average density in the cloud as $\langle\rho\rangle = m/\mathcal{V}$, and the average pressure as $\langle P\rangle = \int_{\mathcal{V}} P d\mathcal{V}/\mathcal{V}$. Fiege & Pudritz

(2000) also state that the effective pressure inside a molecular cloud generally can be written as $P = \rho\sigma^2$. Dividing Equation (2.3) by $\mathcal{V}$ we get

$$0 = 2\langle P\rangle - 2P_S + \frac{\mathcal{W}+\mathcal{M}}{\mathcal{V}},$$

which implies

$$\frac{\langle P\rangle}{P_S} = 1 + \frac{1}{2\langle P\rangle\mathcal{V}}(\mathcal{W}+\mathcal{M}) = 1 + \frac{\mathcal{W}}{2\langle P\rangle\mathcal{V}}\left(1+\frac{\mathcal{M}}{\mathcal{W}}\right) = [\mathcal{W}<0] =$$

$$= 1 + \frac{\mathcal{W}}{2\langle P\rangle\mathcal{V}}\left(1-\frac{\mathcal{M}}{|\mathcal{W}|}\right).$$

Now we focus on the the factor

$$\frac{\mathcal{W}}{2\langle P\rangle\mathcal{V}} = -\frac{m^2G}{2\langle P\rangle\mathcal{V}} = -\frac{Gm}{2\langle P\rangle}\frac{m}{\mathcal{V}} = -\frac{Gm}{2}\frac{\langle\rho\rangle}{\langle P\rangle} = -\frac{Gm}{2\langle\sigma^2\rangle} = -\frac{m}{m_{\rm vir}},$$

where $m_{\rm vir} = 2\langle\sigma^2\rangle/G$ is the virial line mass. Putting all these results together we now get the filamentary virial equation

$$\frac{P_S}{\langle P\rangle} = 1 - \frac{m}{m_{\rm vir}}\left(1-\frac{\mathcal{M}}{|\mathcal{W}|}\right), \tag{2.5}$$

which is exactly equation (11) of Fiege & Pudritz (2000). They further state that the magnetic energy can be written as

$$\mathcal{M} = 2(\langle P_{\rm mag}\rangle - P_{\rm mag,S})\mathcal{V}.$$

Inserting this, as well as the expressions for the virial line mass and the gravitational energy into Equation (2.5) we get

$$\frac{P_S}{\langle P\rangle} = 1 - \frac{m}{m_{\rm vir}} + \frac{\langle P_{\rm mag}\rangle - P_{\rm mag,S}}{\langle P\rangle}. \tag{2.6}$$

2.1.3 Previous studies on filamentary virial analysis

Filamentary virial analyses have been performed by Hernandez et al. (2011a) towards the two filamentary IRDCs G34.43+0.24 and G35.39-0.33 (clouds F and H in the sample of Butler & Tan, 2009, 2012) using ^{13}CO(1-0) line emission data and mass estimates from MIREX mapping. They divided the clouds into seven and four orthogonal strips respectively, within which the analysis was carried out. They found that the envelope to filament pressure ratio to be greater than one within all of the strips. Further, the authors state that such results imply that the filaments have not yet reached virial equilibrium, as long as the pressure measurements are reliable and not severely affected by the assumed filament geometry or other systematic effects.

Hernandez et al. (2011a) also note that the strips with the smallest values of the envelope to filament pressure ratio (their strips F6, F7 and H2) might show indications of more active star formation. Star formation needs gravitationally unstable

conditions to occur, and these results indicate that approximate virial equilibrium is also needed within the local region of the filament, even though surface pressure terms still remain dynamically important.

Cloud H was later revisited by Hernandez et al. (2012). They expanded on the analysis of Hernandez et al. (2011a) by considering two different cases for the filament, an inner and an outer case, while keeping the same strip placement. They also used different data, $C^{18}O$(1-0) and (2-1) line emission data, and updated mass estimates by incorporating near-infrared (NIR) corrections. Their results indicate that (at least) the inner filament is consistent with being in virial equilibrium without the need for large scale net support or confinement from magnetic fields. However, both Hernandez et al. (2011a) and Hernandez et al. (2012) did not have access to estimates of the magnetic field strength and morphology. Thus, they were not able to assess the importance of magnetic fields in their analyses.

2.2 Radiative transfer

Radiative transfer theory describes how radiation propagates through absorbing and emitting media. This is crucial to understand in order to interpret the signals picked up by telescopes. One fundamental quantity within radiative transfer theory is the specific intensity, I_ν, defined as the electromagnetic power per unit area, frequency and solid angle in a given direction (Draine, 2011). Draine (2011) also states that if the radiation field is in local thermodynamic equilibrium (LTE), then the specific intensity will be given by that of a blackbody

$$(I_\nu)_{\mathrm{LTE}} \equiv B_\nu(T) = \frac{2h\nu^3}{c^2}\frac{1}{\exp\left(h\nu/k_{\mathrm{B}}T\right)-1}. \tag{2.7}$$

Also, in thermal equilibrium the relative level populations is given by the Boltzmann distribution

$$\frac{n_u}{n_l} = \frac{g_u}{g_l}e^{-h\nu/k_{\mathrm{B}}T}, \tag{2.8}$$

where n_u and n_l are the number densities in the upper and lower states, and g_u and g_l are the statistical weights of the upper and lower states respectively (Mangum & Shirley, 2015).

The equation governing how the specific intensity changes as the radiation propagates is the equation of radiative transfer

$$dI_\nu = -I_\nu\kappa_\nu ds + j_\nu ds, \tag{2.9}$$

where the first term is due to absorption and stimulated emission, and the second term is due to spontaneous emission (Draine, 2011). Here κ_ν is the attenuation coefficient, given by

$$\kappa_\nu = \frac{c^2}{8\pi\nu^2}\frac{g_u}{g_l}n_l A_{ul}\left(1-\frac{g_l n_u}{g_u n_l}\right)\phi_\nu, \tag{2.10}$$

and j_ν is the emissivity, given by

$$j_\nu = \frac{h\nu}{4\pi}A_{ul}n_u \tag{2.11}$$

(see Mangum & Shirley, 2015, for details). Here A_{ul} is the Einstein coefficient for spontaneous emission, and ϕ_ν is the line profile. It should be noted that the form of the equation of radiative transfer in Equation (2.9) neglects effects from scattering.

Since the path of the path of propagation is not generally known for the radiation measured, it is convenient to introduce the optical depth τ_ν defined as

$$d\tau_\nu \equiv \kappa_\nu ds, \tag{2.12}$$

which means that the radiation propagates in the direction of increasing optical depth (Draine, 2011). With this new independent variable, the equation of radiative transfer becomes

$$dI_\nu = -I_\nu d\tau_\nu + S_\nu d\tau_\nu,$$

where $S_\nu = j_\nu/\kappa_\nu$ is referred to as the source function.

Together with the definition of column density,

$$N = \int n ds, \tag{2.13}$$

we can relate the optical depth to the column density of the lower energy state by combining Equations 2.8, 2.10 and 2.12. Putting everything together and integrating along the path of propagation we get

$$\tau_\nu = \int \kappa_\nu ds = \frac{c^2}{8\pi\nu^2}\frac{g_u}{g_l}A_{ul}\phi_\nu \int n_l(s)\left(1 - \frac{g_l n_u(s)}{g_u n_l(s)}\right) ds =$$

$$= \frac{c^2}{8\pi\nu^2}\frac{g_u}{g_l}A_{ul}\phi_\nu N_l\left(1 - \frac{g_l N_u}{g_u N_l}\right) = \frac{c^2}{8\pi\nu^2}\frac{g_u}{g_l}A_{ul}N_l\left(1 - e^{h\nu/k_\mathrm{B}T}\right)\phi_\nu.$$

Now we integrate this expression in frequency, assuming only the line profile to vary significantly over the line profile, and get

$$\int \tau_\nu d\nu = \frac{c^2}{8\pi\nu^2}\frac{g_u}{g_l}A_{ul}N_l\left(1 - e^{h\nu/k_\mathrm{B}T}\right)\int \phi_\nu d\nu = \frac{c^2}{8\pi\nu^2}\frac{g_u}{g_l}A_{ul}N_l\left(1 - e^{h\nu/k_\mathrm{B}T}\right),$$

where we have used the fact that $\int \phi_\nu d\nu = 1$. Making the variable substitution $d\nu = \frac{\nu}{c}dv$ we can isolate the lower state column density as

$$N_l = \frac{8\pi\nu^3}{A_{ul}c^3}\frac{g_l}{g_u}\left(1 - e^{h\nu/k_\mathrm{B}T}\right)^{-1}\int \tau_\nu dv. \tag{2.14}$$

The total column density is related to the lower state column density as

$$N_\mathrm{tot} = \frac{Q_\mathrm{rot}}{g_l}e^{E_l/k_\mathrm{B}T}N_l. \tag{2.15}$$

Putting Equation (2.14) into Equation (2.15) we finally get the total column density as

$$N_\mathrm{tot} = \frac{8\pi\nu^3}{A_{ul}c^3}\frac{g_l}{g_u}\frac{1}{1 - e^{h\nu/k_\mathrm{B}T}}\frac{Q_\mathrm{rot}}{g_l e^{-E_l/k_\mathrm{B}T}}\int \tau_\nu dv. \tag{2.16}$$

2.3 Depletion

In cold ($T \lesssim 20$ K) environments, CO is expected to freeze out onto dust grains (see e.g. Tan et al. (2014)). This freeze out lends less of the CO to remain in the gas phase where it is able to be directly observed through its rotational line emissions. CO (and its isotopologues) are readily used to map the interstellar H_2 (Caselli et al., 1999). It is thus of great importance to know the degree of depletion in order to get accurate estimates of the H_2 column density. Furthermore, the depletion of gaseous species by freezing out onto dust grains also alters the the chemical and physical properties of molecular clouds. For instance, Goldsmith & Langer (1978) found that ^{12}CO is the dominant coolant in environments with molecular hydrogen densities $n(H_2) < 3 \cdot 10^4$ cm^{-3}, and kinetic temperatures between 10 K and 40 K. They also state that CI, O_2, and rarer isotopologues of CO contribute significantly to the cooling. Thus, if much of the CO were to be depleted, the thermal balance of such clouds would be affected.

2.3.1 Previous studies on CO depletion in IRDCs

Hernandez et al. (2011b) studied the state of Cloud H using C^{18}O(1-0) and (2-1) line emission data. From this they computed the mass surface density, $\Sigma_{C^{18}O}$, which was found to reach values of ~ 0.07 g/cm^2. The values obtained through this analysis were then compared to mass surface densities derived from MIREX mapping, Σ_{SMF}, in order to get estimates of the depletion factor. Due to the uncertainties in their methods, Hernandez et al. (2011b) renormalize the depletion factors to be, on average, one in regions where $0.01 < \Sigma_{SMF}/(g/cm^2) < 0.03$. After this renormalization, the resulting depletion factors were reported to reach ~ 5, with typical values of $\sim 2 - 3$ along the filament. They thus conclude that widespread CO depletion occurs within the cloud.

Hernandez et al. (2012) also studied CO depletion towards Cloud H. They incorporated mass surface density estimates from both MIR and NIR extinction mapping. Using otherwise the same methods as Hernandez et al. (2011b), they found similar values for the renormalized depletion factor. It is still peaked at ~ 5, and along most of the filament spine it takes values in the range $\sim 2 - 3$.

3
Data & Methods

In this chapter the data used in this project is presented, as well as the methods and assumptions made for the filamentary virial analysis. The methods for the depletion calculations are also described. Finally, the methods for estimating a potential offset between the different datasets are presented.

3.1 Data

As part of this work data from several different telescopes have been used, and these data are briefly described in this section.

3.1.1 SOFIA-HAWC+

Polarized dust emission was observed towards Cloud C as part of the Polarized Light from Massive Protoclusters (POLIMAP, PI: J. C. Tan) survey. The original goal of this survey was to map polarized dust continuum emission towards ten IRDCs (clouds A through J in the sample of Butler & Tan, 2009, 2012), in order to better constrain the the magnetic field properties of IRDCs. Observations were made using the HAWC+ instrument (Harper et al., 2018) aboard the Stratospheric Observatory for Infrared Astronomy (SOFIA). POLIMAP uses 214 μm observations (Project ID: 09-0104), with complementary Green Bank Telescope (GBT)-Argus ^{13}CO(1-0) and C^{18}O(1-0) observations to probe gas kinematics. Prior to the shutdown of SOFIA, POLIMAP HAWC+ observations were made towards clouds B, C, F, H, I, and J, with GBT having observed clouds B, C, F, G, H, I, and J.

The observations of Cloud C were carried out on September 21, 27 and 28, 2022, as part of SOFIA Cycle 9. The beam had a full width at half maximum (FWHM) of 18.2″, and the surveyed area has a size of $12.0' \times 11.4'$. For further details on the instrument, observations, and the methods of data reduction, see Law et al. (2024).

3.1.2 GBT-C^{18}O data

C^{18}O(1-0) emission of the IRDC was observed with Argus onboard the Green-Bank Telescope (GBT) (Sieth et al., 2014) in January to April 2022. ARGUS is a 16-element heterodyne 'radio camera' operating with the GBT in the 85-116 GHz range. ARGUS has 16 heterodyne pixel receivers mounted in a 4×4 layout and with a beam separation of 30.4″ in both the elevation and cross-elevation directions. For further

details on the observations and data reduction, see Law et al. (2024). The resulting data has a spatial resolution of $\sim 7''$ and a spectral resolution of 0.187 km/s.

3.1.3 Archival extinction and mass surface density maps

Archival mass surface density maps are also retrieved for the analysis present in this work. Lim et al. (2016) derive a mass surface density map (Σ-map) by performing graybody fits to Herschel-PACS and SPIRE Far-infrared (FIR) data at 160, 250, 350, and 500 μm (Figure 3.4 top left panel). Our analysis uses the map derived from the galactic Gaussian (GG) foreground-background subtraction method. The readers are referred to the reference for detailed methods and discussion on the construction of the maps.

Mass surface density inferred from mid-infrared (MIR) extinction (MIREX) mapping is also included in this work (see Figure 3.4, middle left panel). This was first done by Butler & Tan (2012) utilizing Spitzer-IRAC 8 μm image data. This map was later improved by Kainulainen & Tan (2013), who applied near-infrared (NIR) corrections, improving the accuracy of the large-scale, lower column density base level of the map. These MIREX maps have a relatively high angular resolution at $2''$, set by the Spitzer-IRAC resolution.

3.1.4 ALMA continuum and $C^{18}O$ data

As part of this work, both 1.3 mm continuum and $C^{18}O$(2-1) spectral line data taken in band 6 of the Atacama Large Millimeter and sub-millimeter Array (ALMA) have been used. The continuum observations were carried out in June 2016 (ALMA cycle 3), and consisted of 86 pointings, covering the majority of the central, dark regions of the IRDC (Kong et al., 2018). The synthesized beam size is $\sim 0.6'' \times 0.4''$, and the pixel size of the data is $0.05''$. The $C^{18}O$(2-1) data cube used in this work instead has an effective beam of $\sim 1.5'' \times 1.0''$, pixel scale of $0.18''$, and a spectral resolution of 0.16 km/s. Both these sets of data were gathered as part of project 2015.1.00183.S (PI: Kong). For more information on the data acquisition, see Kong et al. (2018) and Kong et al. (2019b).

3.2 Offset analysis

Early on when trying to identify filamentary structures in the Spitzer extinction map, and then checking if they appear in the GBT $C^{18}O$(1-0), a potential systematic offset was seen between the two maps, see Figure 3.1. Since such an offset could alter the result from subsequent analyses, some effort was put into quantifying this potential offset, as well as checking other structures for similar trends. These checks were done in a few different ways. First, the elongated structure was analyzed, and the methods used for estimating the offset, as well as the results, can be found in Section 3.2.1.

Another way of checking for the potential offset was carried out by looking for peaked structures in the ALMA continuum image, and then checking for corresponding emission in the ALMA $C^{18}O$(2-1) and GBT $C^{18}O$(1-0) data. The offset

estimation was then made by constructing radial profiles of the $C^{18}O$ data sets around the continuum peak positions. How these radial profiles were created, how they were used for estimating offset, and the results, can be found in Section 3.2.2.

3.2.1 Linear structure offset estimation

In order to be able to estimate the offset between two structures it must first be known which pixels in the data belong to the structure. For elongated structures this was accomplished by extracting pixels with values higher than a certain threshold. From these extracted pixels a spine was retrieved as the pixels that had the maximum value in its row or column in the data. Once spines had been extracted from two data sets, for the same structure, the offset was estimated in a few ways.

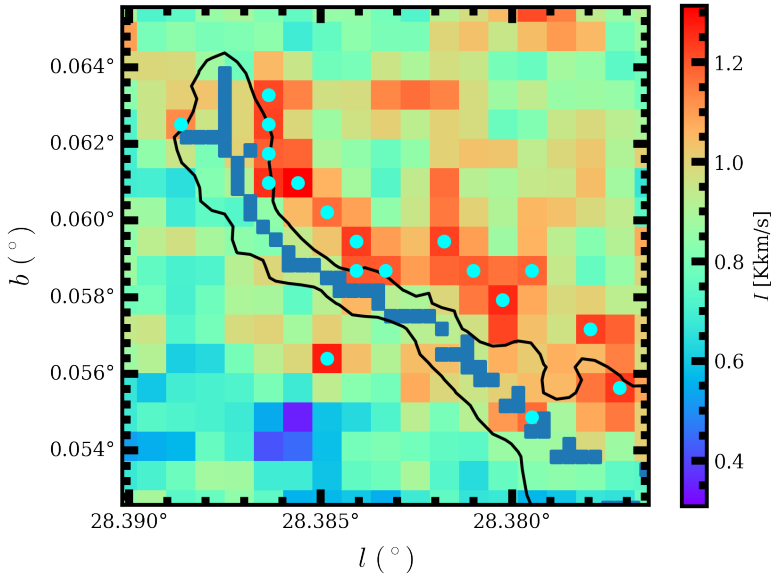

Figure 3.1: Extracted spines for offset estimation from the extinction map (blue squares) and the GBT $C^{18}O$ integrated intensity map (cyan dots, map in background). Also shown is the 65 mag contour from the extinction map.

A first way was to compare the distances of all the pixels in one spine to all the pixels in the other spine, and then taking the shortest distance for each pixel as a measure of the offset. This has the drawback that the direction of the offset not necessarily will be the same for each pixel. Thus, another way of estimation is needed in order to see a systematic direction of the offset.

Another way was to check the offset along a certain direction. For this, the pixels in one of the spines was compared to the pixels in the other spine. The pixel in the second spine that is closest to the direction of interest was then used for estimating the offset. This was then done for all of the pixels in the first spine and a distribution of offsets was obtained.

The spines extracted from the GBT $C^{18}O$ and Spitzer extinction data for the identified linear structure can be seen in Figure 3.1. It can be seen that the points in the $C^{18}O$ spine (cyan dots) generally to the north-west of the extinction spine

(blue squares). The offset was quantified in a few different, as stated in above: 1) As the minimum absolute distance from the spine pixels of the $C^{18}O$ data to any pixel within the extinction spine. 2) Along certain directions, here taken to be purely in longitude, purely in latitude, and perpendicular to the extinction spine (with direction measured from a linear fit to the extinction spine). Resulting offset histograms can be seen in Figure 3.2. It should be noted that the offsets computed perpendicular to the extinction spine were defined as positive/negative if the corresponding longitude offset was positive/negative. It can be seen that there is significant spread in the offset magnitudes in all cases. There seems to be a peak around $-5''$ for the longitude and perpendicular cases, while it is less clear in the latitude case. The minimum absolute offset case show no peak in its distribution. From these results, there is no clear evidence for a systematic offset between the two sets of data.

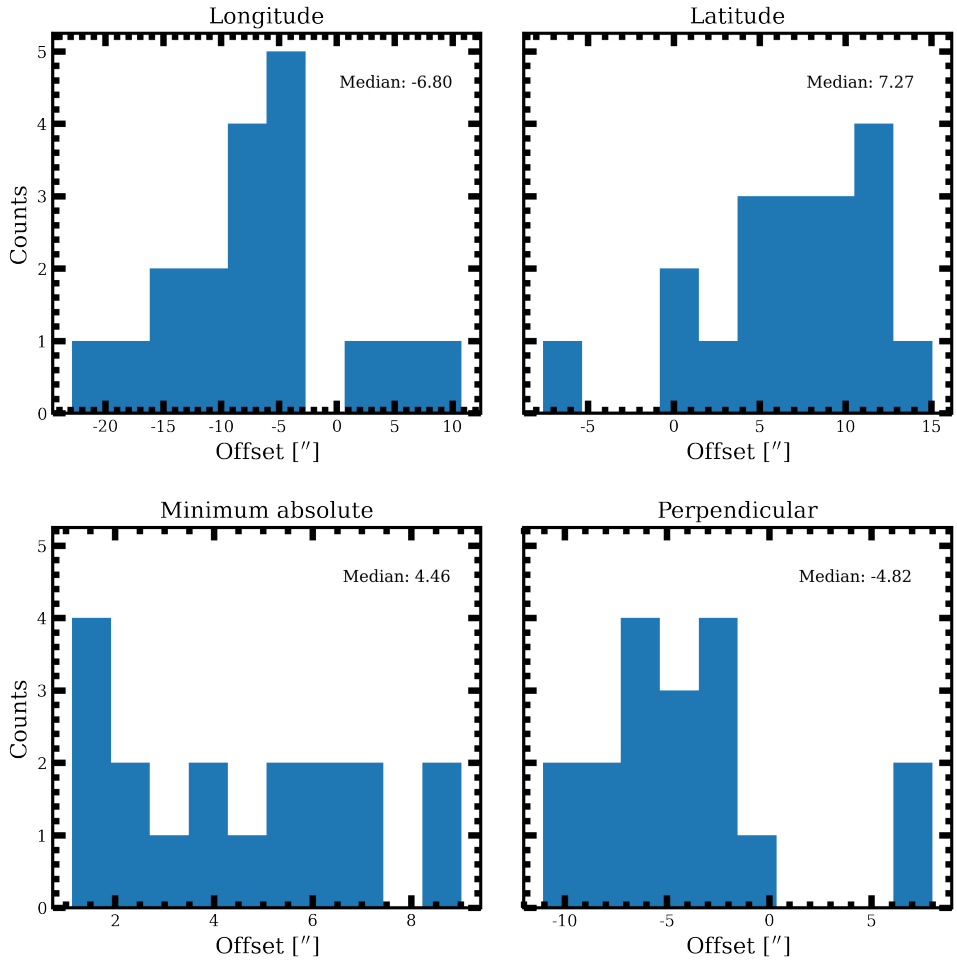

Figure 3.2: Histograms of the computed offsets between the spines extracted from the GBT $C^{18}O$ integrated intensity map and the extinction map (cyan dots and blue squares respectively in Figure 3.1). Top left: Offsets computed along the galactic longitude direction. Top right: Offsets computed along the galactic latitude direction. Bottom left: Minimum absolute offsets. Bottom right: Offsets computed in the direction perpendicular to the extinction spine. In the top right of each panel the median of the corresponding distribution can be found.

3.2.2 Offset estimation using radial profiles

Radial profiles were made by extracting data from a number of concentric annuli of fixed width. The innermost "annulus" was taken to be a circle with radius matching the width of the rest of the annuli. The data within these annuli were extracted using the package *regions* in python (Bradley et al., 2022). There are a few modes to select from when making the extractions, the two main ones considered in this analysis being "exact" and "center". The difference between these two modes is that in exact mode, the fraction of a pixel that is withing a region is taken into account, and the pixels are thus given an appropriate weight between zero and one, while in center mode all pixels which have their center within the region get the weight one, and all other pixels get the weight zero (Bradley et al., 2022). The exact mode can thus be useful if an average radial profile is wanted, while the center mode is useful if the maximum within each region is of interest. The data from the extracted annuli can then be manipulated (i.e. averaged, searched for the maximum, etc.) in order to achieve the radial profile.

For the offset estimation integrated intensity maps of the ALMA $C^{18}O$(2-1) and GBT $C^{18}O$(1-0) were used, where the integration interval varied between the different peak positions. The radial profiles were centered on the continuum peaks using the center mode, and the annulus width was taken to be one pixel width for the data in question ($\sim 0.18''$ for the ALMA data, $\sim 2.75''$ for the GBT data). The maximum value within each annulus was found, and the coordinates of the corresponding pixels were saved. That the maximum was used was due to the desire of finding peaked structures, which could have been averaged out over the larger area of the annuli otherwise. The peak positions were then identified by comparing the integrated intensity maps and the radial profiles. Once the peaks had been identified the magnitude and direction of the offset were calculated from the continuum peak to the ALMA $C^{18}O$(2-1) peak, as well as from the ALMA $C^{18}O$(2-1) peak to the GBT $C^{18}O$(1-0) peak. The direction was defined as the angle between the the north axis and the line connecting the two points, also known as the position angle (PA). This angle ranges between 0° and 360°, with 90° being towards the east, and 270° being towards the west.

In total, four continuum peaks with seemingly corresponding ALMA $C^{18}O$(2-1) and GBT $C^{18}O$(1-0) emission were considered for the offset estimation. One of these continuum peaks is shown in Creffig:peak1 (top left) (the other three are shown in Figures A.1, A.2, and A.3 in Appendix A), together with integrated intensity maps of the GBT $C^{18}O$(1-0) (bottom left), ALMA $C^{18}O$(2-1) (top right), and ALMA $C^{18}O$(2-1) regridded to the same pixel scale and velocity channels as the GBT data (bottom right).

The resulting offsets and corresponding directions, as well as the peak positions considered, are shown in Table 3.1. It can be seen that the distances between the continuum and ALMA $C^{18}O$ peaks (d_{cont}) are smaller than the distance between the ALMA and GBT $C^{18}O$ peaks ($d_{C^{18}O}$). There is also some spread in the computed distances, possibly hinting towards there not being any systematic offset. Also worthy to note are the position angles between the extracted peaks (θ_{cont} and $\theta_{C^{18}O}$). The values of these span a large range of angles ($7° - 212°$), indicating that the offsets are in different directions for the different peaks. This further points towards there

not being a systematic offset between the sets of data. However, a larger sample would be needed to say anything for certain.

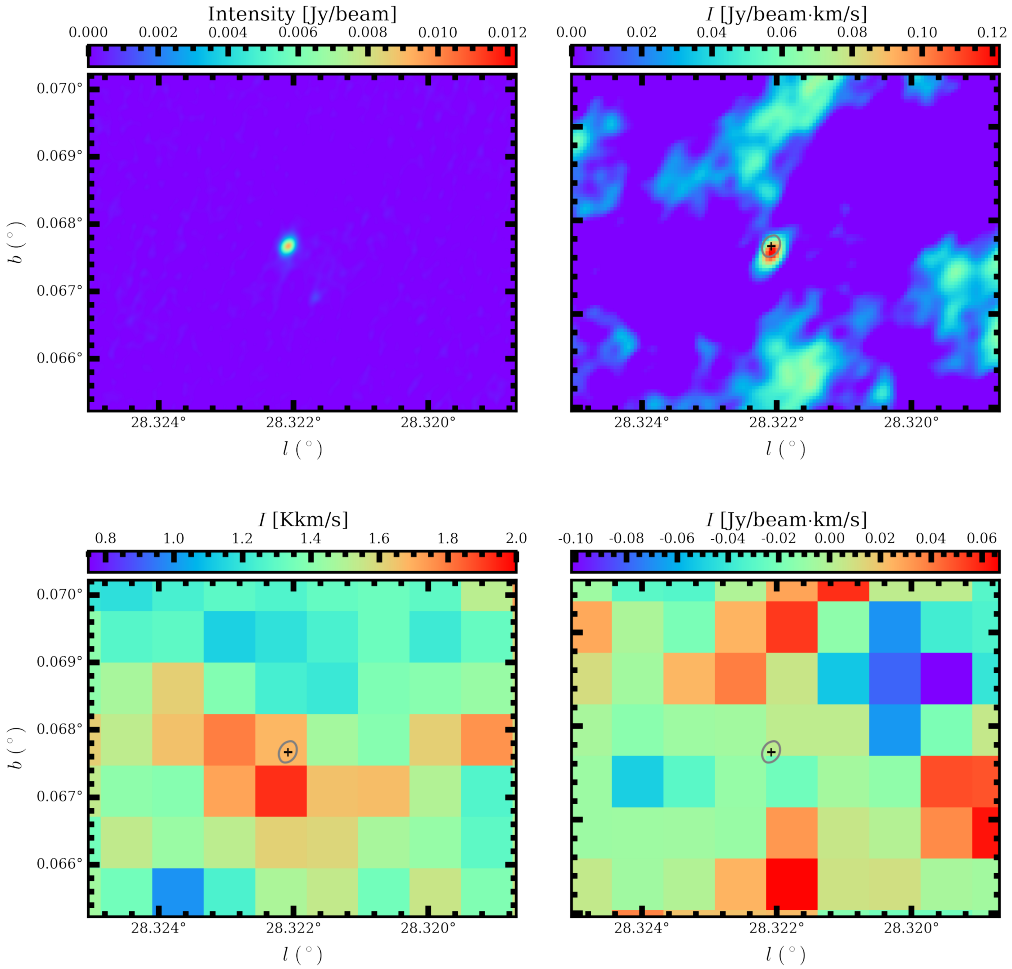

Figure 3.3: Top left: ALMA continuum image of peak 1 (seen in the center, and marked by the black plus in the other panels). Bottom left: GBT $C^{18}O$(1-0) integrated intensity. Top right: ALMA $C^{18}O$(2-1) integrated intensity (78.0 − 79.0 km/s). Bottom right: ALMA $C^{18}O$(2-1) integrated intensity regridded to match the spatial pixel scale of the GBT $C^{18}O$(1-0) emission. In all panels except the top left, a contour from the ALMA continuum image at 0.002 Jy/beam is overlaid.

Table 3.1: Positions (galactic longitude and latitude) of some continuum (columns 2 and 3), ALMA $C^{18}O$(2-1) (columns 4 and 5), and GBT $C^{18}O$(1-0) (columns 6 and 7) emission peaks (column 1), as well as position angles and distances between the different peaks (continuum-$C^{18}O$(2-1) in columns 8 and 9, and $C^{18}O$(2-1)-$C^{18}O$(1-0) in columns 10 and 11).

Peak	l_{cont} (°)	b_{cont} (°)	l_{2-1} (°)	b_{2-1} (°)	l_{1-0} (°)	b_{1-0} (°)	θ_{cont} (°)	d_{cont} (″)	$\theta_{\mathrm{C^{18}O}}$ (°)	$d_{\mathrm{C^{18}O}}$ (″)
1	28.3221	0.0677	28.3221	0.0676	28.3222	0.0671	174	0.35	169	1.79
2	28.3429	0.0605	28.3427	0.0597	28.3420	0.0587	195	2.93	212	4.41
3	28.3478	0.0588	28.3481	0.0589	28.3482	0.0579	68	1.02	176	3.45
4	28.3656	0.0519	28.3656	0.0519	28.3657	0.0526	146	0.23	7	2.53

3.3 Filamentary virial analysis

In order to do the filamentary virial analysis, the main part of the cloud was divided into 14 strips. These strips were taken to have a width of 18″, corresponding to a physical scale of 0.44 pc in the plane of the sky at a distance of 5 kpc, and matching the spatial resolution of the Herschel mass surface density map. Within each of these strips an outer and an inner filament region were defined. The outer filament regions were all taken to be centered at a galactic latitude of 0°03′40.9″, and given a height of 2′. The inner filament regions were then taken to be centered at the center of mass of the main part of the cloud, while having a height of 1′. The centers of mass were calculated iteratively from the mass surface density map from Herschel. In the first iteration, the center of mass of the outer filament region was computed. From the second iteration onward, a region of the same height as the inner filament region, centered on the center of mass of the last iteration, was used to compute the new center of mass. This process was then applied until the center of mass either did not move by a significant amount between consecutive iterations, it got stuck jumping back and forth, or a maximum number of iterations was reached. The resulting regions can be seen overlaid on the different data in Figure 3.4. For each of the inner and outer filament regions, corresponding envelope regions were defined to the north and south. In both the inner and outer cases, the envelope regions were taken to extend an extra 30″ from the filament boundary. This was chosen to be consistent with the ratios of the outer radii to the filament radii of Hernandez et al. (2012) (2 for the inner filament, and 1.5 for the outer filament).

3.3.1 Filament geometry and envelope subtraction

Since the detailed geometry of the filament is not known, it is assumed to be locally cylindrical, with radius R_f, within a cylindrical envelope, with outer radius R_e and inner radius R_f, following the assumptions and notation of Hernandez et al. (2012). A cross section of the filament with this geometry can be seen in Figure 3.5. The envelope can now be divided into three parts, one overlapping with the filament along the line of sight, and two where it does not overlap (called "on" and "off" regions respectively, see Figure 3.5). In order to get the properties of the filament, the envelope has to be subtracted off from the total in the "on" region. Take the case of mass surface density first. It can be directly measured for the envelope "off" regions, $\Sigma_{e,\mathrm{off}}(N)$ and $\Sigma_{e,\mathrm{off}}(S)$ (assuming negligible other foreground and background). We now want to derive an equation relating the average envelope "off" region mass surface density, $\bar{\Sigma}_{e,\mathrm{off}}$, to the to the average of the envelope as a whole. This is possible assuming an envelope of uniform density, ρ_e, as was done in Hernandez et al. (2012). The average mass surface density within a region can then be expressed as

$$\bar{\Sigma} = \frac{\rho V}{A},$$

where ρ is the density of the region, V is the volume of the region, and A is the projected area on the plane of the sky of the region. Assuming the envelope to be a cylindrical shell (as described above) of height h we get $V_e = \pi(R_e^2 - R_f^2)h$ and

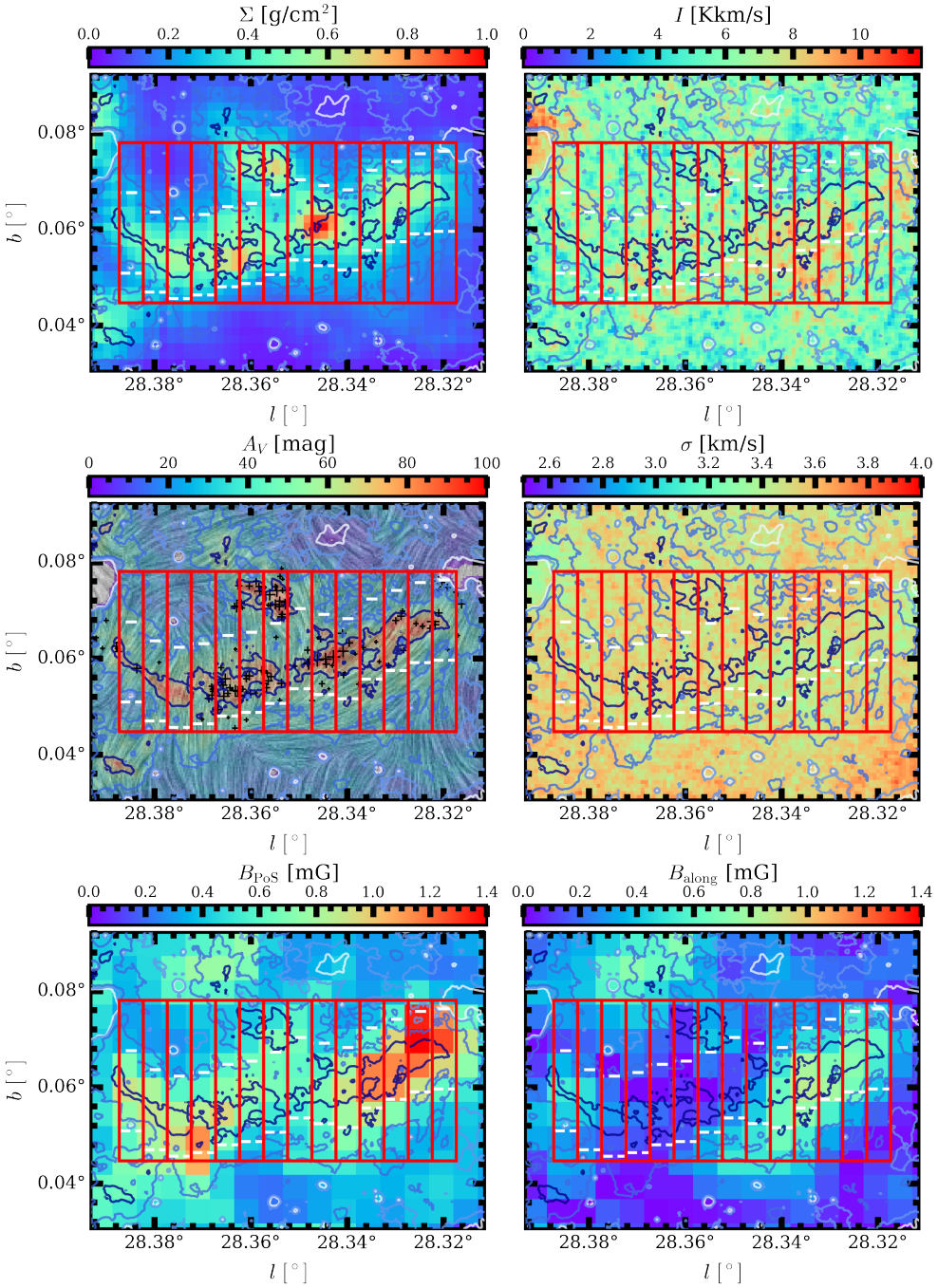

Figure 3.4: Top left: Herschel mass surface density map. Top right: GBT $C^{18}O$ integrated intensity map. Middle left: Spitzer MIR extinction map with positions of detected ALMA continuum sources marked as black plus signs. The larger the marker appears, the more massive the source was estimated to be. Overlaid as a drapery is the inferred plane of sky magnetic field component. Middle right: Velocity dispersion map from Law et al. (2024). Bottom left: Plane of sky magnetic field strength map. Bottom right: Map of the magnetic field component along the filament (i.e. in the east-west direction). In each panel, the inner and outer filament regions are overlaid as dashed white and solid red lines, respectively, as well as MIR extinction contours at A_V = 7, 15, 30, 60 mag.

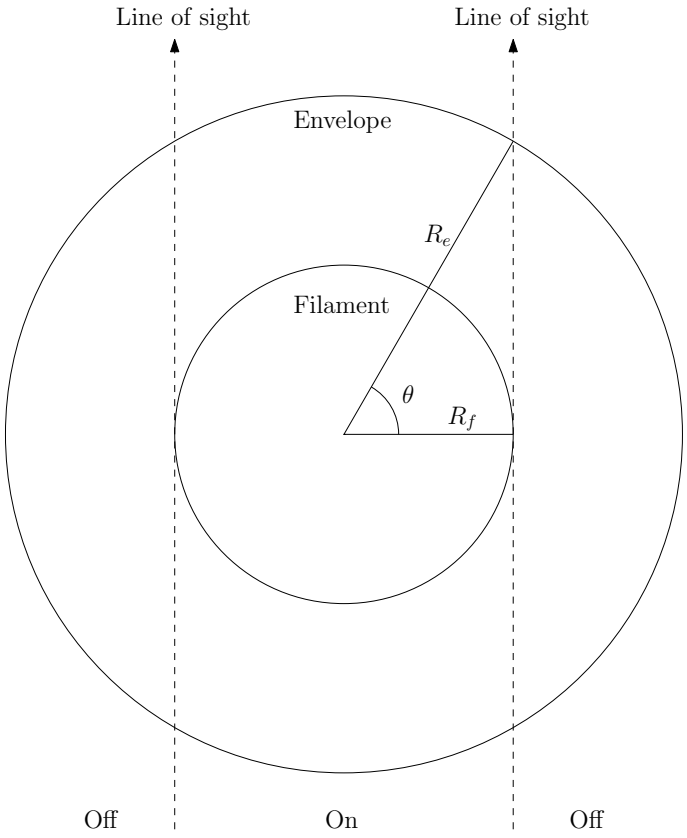

Figure 3.5: Schematic view of a cross section of the filament and its envelope.

$A_e = 2R_e h$ for the envelope as a whole. The volume of the off regions is less trivial. It is the area of two circular sector of angle 2θ, i.e. $2\theta R_e^2$, minus the area of two isosceles triangles, $2R_f\sqrt{R_e^2 - R_f^2}$, all multiplied by the height of the cylinder. Thus, for the "off" regions we get $V_{e,\text{off}} = 2\left(\theta R_e^2 - R_f\sqrt{R_e^2 - R_f^2}\right)h$, and $A_{e,\text{off}} = 2(R_e - R_f)h$. Putting all this together we then get

$$\bar{\Sigma}_e = \rho_e \frac{\pi}{2}\frac{R_e^2 - R_f^2}{R_e}, \tag{3.1}$$

and

$$\bar{\Sigma}_{e,\text{off}} = \rho_e \frac{\theta R_e^2 - R_f\sqrt{R_e^2 - R_f^2}}{R_e - R_f}. \tag{3.2}$$

We now take the ratio of these two mass surface densities, which gives us

$$\frac{\bar{\Sigma}_e}{\bar{\Sigma}_{e,\text{off}}} = \frac{\pi}{2}\frac{R_e^2 - R_f^2}{R_e} \cdot \frac{R_e - R_f}{\theta R_e^2 - R_f\sqrt{R_e^2 - R_f^2}} =$$

$$= \pi\frac{R_e^2 - R_f^2}{R_e^2}\frac{R_e - R_f}{R_e}\left(2\theta - 2\frac{R_f}{R_e}\frac{\sqrt{R_e^2 - R_f^2}}{R_e}\right)^{-1}.$$

From Figure 3.5 we can see that $\cos(\theta) = R_f/R_e$ and $\sin(\theta) = \sqrt{R_e^2 - R_f^2}/R_e$. This gives us

$$\frac{\bar{\Sigma}_e}{\bar{\Sigma}_{e,\text{off}}} = \pi \sin^2(\theta)(1 - \cos(\theta))(2\theta - 2\cos(\theta)sin(\theta))^{-1}.$$

Finally the average mass surface density of the entire envelope can then be calculated as

$$\bar{\Sigma}_e = \frac{\pi \sin^2(\theta)(1 - \cos(\theta))}{2\theta - \sin(2\theta)} \bar{\Sigma}_{e,\text{off}}. \tag{3.3}$$

Note that Equation (3.3) is precisely Equation (1) of Hernandez et al. (2012). From this result we get the average mass surface density of the envelope "on" region as

$$\bar{\Sigma}_{e,\text{on}} = \frac{R_e}{R_f}\bar{\Sigma}_e - \frac{R_e - R_f}{R_f}\bar{\Sigma}_{e,\text{off}}. \tag{3.4}$$

In our cases we have $R_e/R_f = 2$ for the inner regions, and $R_e/R_f = 1.5$ for the outer regions. This gives $\bar{\Sigma}_{e,\text{on}}/\bar{\Sigma}_{e,\text{off}} = 0.918$ and 0.768 for the inner and outer regions respectively. The mass surface density of the filament is then given by

$$\bar{\Sigma}_f = \bar{\Sigma}_{\text{on}} - \bar{\Sigma}_{e,\text{on}}. \tag{3.5}$$

It should be noted that for strip 1, the envelope was estimated from only the northern part to avoid the spur to the south. Similarly, for the inner case of strips 5-8, only the southern envelope was used for the subtraction in order to avoid the spur to the north. This was only done for the mass surface densities.

3.3.2 Relevant parameters

In order to see if the data is consistent with the model of virial equilibrium by Fiege & Pudritz (2000), described in Section 2.1.2, some parameters have to be calculated. The mass surface densities of the envelope "off" regions were computed directly from the Herschel mass surface density map as area weighted averages. For the "on" regions, the mass surface densities were computed as described in Section 3.3.1. In the case of no envelope subtraction, the filament mass surface density was taken to be the area weighted average of the "on" region instead ($\bar{\Sigma}_f = \bar{\Sigma}_{\text{on}}$). From these values, the masses were calculated by multiplying by the area in the plane of the sky of the respective region. The line masses and densities were then calculated by dividing the mass by the length along the filament and volume respectively of the respective region. For the length, it is assumed that the filament is observed at an inclination of $i = 60° \pm 15°$ (90° would be in the plane of the sky), following the assumptions of Hernandez et al. (2012). The gravitational energy per unit length was then calculated according to Equation (2.4).

In order to compute the pressures of the filament and envelope regions, $C^{18}O(1-0)$ data from GBT was used. The central velocity, v_c, and the velocity dispersion, σ, were computed by the first and second order moments from the spectra

$$v_c = \frac{\int Ivdv}{M_0},$$

$$\sigma^2 = \frac{\int I(v - v_c)^2 dv}{M_0},$$

where M_0 is the zeroth moment, i.e. the integrated intensity

$$M_0 = \int I dv.$$

For the envelope regions, I is the average spectrum from the north and south envelope regions. For the filament, it is taken to be the average spectrum from the "on" regions in the case without envelope subtraction. In the case with envelope subtraction, the filament spectra were computed in the same way the filament mass surface densities were. However, when calculating the different moments, all values below zero in the subtracted spectra were neglected.

The magnetic field strength was estimated from the refined DCF method map of Law et al. (2024). To get a field strength estimate in the filaments, the area weighted average was computed for the "on" regions. For the magnetic pressure, the map was first squared, and then an area weighted average was computed. The magnetic pressure was then computed as

$$\langle P_{\rm mag} \rangle = \frac{(B^2)_{av,on}}{8\pi},$$

(see e.g. Draine, 2011). Since the exact magnetic field structure is not resolved, the magnetic surface pressure was computed in the same way, but for the data of the envelope off regions. However, it is also scaled as the mass surface density is in Equation (3.3).

3.4 Depletion analysis

For the calculations of the $C^{18}O$ depletion factors, f_D, the analysis of Hernandez et al. (2011a) is followed. The depletion factor is defined as

$$f_D = \frac{N^{\rm exp}_{C^{18}O}}{N^{\rm obs}_{C^{18}O}}, \tag{3.6}$$

where $N^{\rm exp}_{C^{18}O}$ and $N^{\rm obs}_{C^{18}O}$ are the expected and observed column densities of $C^{18}O$ respectively. The expected column density is derived in two different ways. One is from the mass surface density map by assuming a mass per hydrogen nucleus $\mu_{\rm H} = 2.34 \cdot 10^{-24}$ g, and an abundance ratio of $C^{18}O$ to H_2 of $6.12 \cdot 10^{-7}$ (same values as assumed in Hernandez et al. (2011a)). Assuming all Hydrogen is in the form of H_2, the expected column density of $C^{18}O$ can be calculated as

$$N^{\rm exp}_{C^{18}O} = 6.12 \cdot 10^{-7} \frac{\Sigma_{\rm tot}}{2\mu_{\rm H}}. \tag{3.7}$$

The other way is by converting the extinction map to hydrogen column density, for which the same conversion as Kainulainen & Tan (2013) is adopted:

$$N_{\rm H} = 1.9 \cdot 10^{21} {\rm cm}^{-2} \left(\frac{A_V}{\rm mag} \right).$$

This column density of hydrogen is then converted to $C^{18}O$ column density by multiplying by the same factor as stated above.

The observed column density of $C^{18}O$ can be derived from the general equation (Equation (1) of Hernandez et al. (2011a))

$$\frac{\mathrm{d}N^{\mathrm{obs}}_{\mathrm{C^{18}O}}(v)}{\mathrm{d}v} = \frac{8\pi}{A\lambda_0^3}\frac{g_l}{g_u}\frac{\tau_\nu}{1-\exp\left(-h\nu/k_\mathrm{B}T_\mathrm{ex}\right)}\frac{Q_\mathrm{rot}}{g_l\exp\left(-E_l/k_\mathrm{B}T_\mathrm{ex}\right)}. \tag{3.8}$$

Here A is the Einstein coefficient, λ_0 is the rest wavelength of the transition, g_l and g_u are the lower and upper state degeneracies of the transition ($g_J = 2J+1$), τ_ν is the optical depth of the line at frequency ν, h is the Planck constant, k_B is the Boltzmann constant, T_ex is the excitation temperature, Q_rot is the partition function, and E_l is the energy of the lower state of the transition. In the case of $C^{18}O$, the partition function is that of linear molecules and is given by

$$Q_\mathrm{rot} = \sum_{J=0}^{\infty}(2J+1)\exp\left(-E_J/k_\mathrm{B}T_\mathrm{ex}\right). \tag{3.9}$$

Here $E_J = J(J+1)hB$ is the energy of the rotational state with quantum number J, and $B = 54.891$ GHz being the rotational constant of the $C^{18}O$ molecule.

The optical depth cannot be observed directly, but it can be derived from the detection equation (Equation (2) of Hernandez et al. (2011a)):

$$T_{B,\nu} = \frac{h\nu}{k_\mathrm{B}}(f(T_\mathrm{ex}) - f(T_\mathrm{bg}))(1-e^{-\tau_\nu}), \tag{3.10}$$

with $T_{B,\nu}$ being the main beam brightness temperature at frequency ν, T_bg is the cosmic microwave background temperature of 2.73 K, and $f(T) = (\exp\left(h\nu/k_\mathrm{B}T\right) - 1)^{-1}$. In the optically thin limit (τ_ν small) it holds that $e^{-\tau_\nu} \approx 1-\tau_\nu$, and τ_ν can be computed as

$$\tau_\nu = T_{B,\nu}\frac{k_\mathrm{B}}{h\nu}\frac{1}{f(T_\mathrm{ex}) - f(T_\mathrm{bg})} \tag{3.11}$$

for an observed $T_{B,\nu}$ and assumed T_ex.

In the case of this study, the $C^{18}O(J = 1-0)$ rotational transition is used, for which the relevant parameters are listed below.

- $A = 6.266 \cdot 10^{-8}$ s^{-1}
- $\lambda_0 = 2.731$ cm
- $\nu = 109.78$ GHz
- $g_l = 1,\ g_u = 3$
- $E_l = 0$

The above values were taken from the Cologne Database for Molecular Spectroscopy (CDMS, Müller et al., 2005).

4

Results

In this chapter the results of the filamentary virial analysis, depletion analysis, and offset estimation are presented.

4.1 Filamentary virial analysis

As mentioned in Section 3.3, several different cases of envelope subtraction were considered: 1) No envelope subtraction. 2) Mass surface densities envelope subtracted, but not the spectra. 3) Mass surface densities and spectra envelope subtracted. In all three cases the same geometrical considerations were made regarding the filament and its envelope (see Section 3.3.1 for details). These three cases are also paired with different amounts of consideration of the magnetic fields. Firstly, the magnetic fields are not considered. Secondly, only the "on" region magnetic pressures were considered. Lastly, both the "on" region and surface magnetic pressures were taken into account.

The spectra from the different strips can be seen in Figures 4.1-4.8. The left panel of each figure shows the total observed spectra for the "on" regions (solid red line), together with the spectra of the north and south envelope regions (dashed blue and dot-dashed brown lines respectively). The right panel instead shows the total "on" region spectra (solid red), as well as the scaled mean envelope spectra (dashed blue) and the envelope subtracted filament spectra (solid black). Figures 4.1-4.4 show the results for the inner strip regions, while Figures 4.5-4.8 are for the outer strip regions. It can be seen that the envelope spectra are in general similar in strength to the "on" region spectra, resulting in the envelope subtracted spectra having quite low peak intensities in comparison. Another thing to note is that the spectra from the northern and southern envelope regions can have markedly different appearance. Some striking examples of this can be seen in Figure 4.7, where the south envelope regions can be seen to have a peak at around 75 km/s, while this is completely missing from the north envelope regions.

For the analysis without any envelope subtraction, the total spectrum of the "on" regions were used. In the case with envelope subtraction, the envelope subtracted spectra of Figures 4.1-4.8 were used first after setting all negative values to zero. This was done in order to get more reliable results, since the computed second moment (that is the square of the velocity dispersion) became negative otherwise.

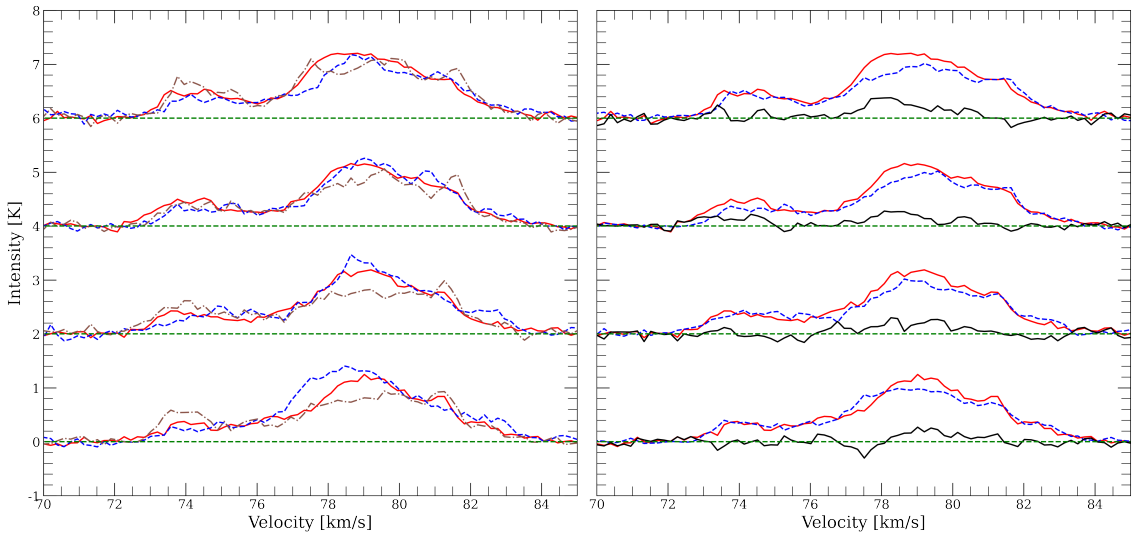

Figure 4.1: Spectra for the inner strip regions for strips 1-4 (bottom to top). The red solid lines in both panels are the spectra extracted from the "on" regions, and the green dashed lines show the respective zero-points for the different spectra. The left panel also shows the spectra from the north and south envelope regions (dashed blue and dot-dashed brown respectively). The right panel also shows the scaled average spectra of the envelope regions (dashed blue), and the envelope subtracted filament spectra (solid black).

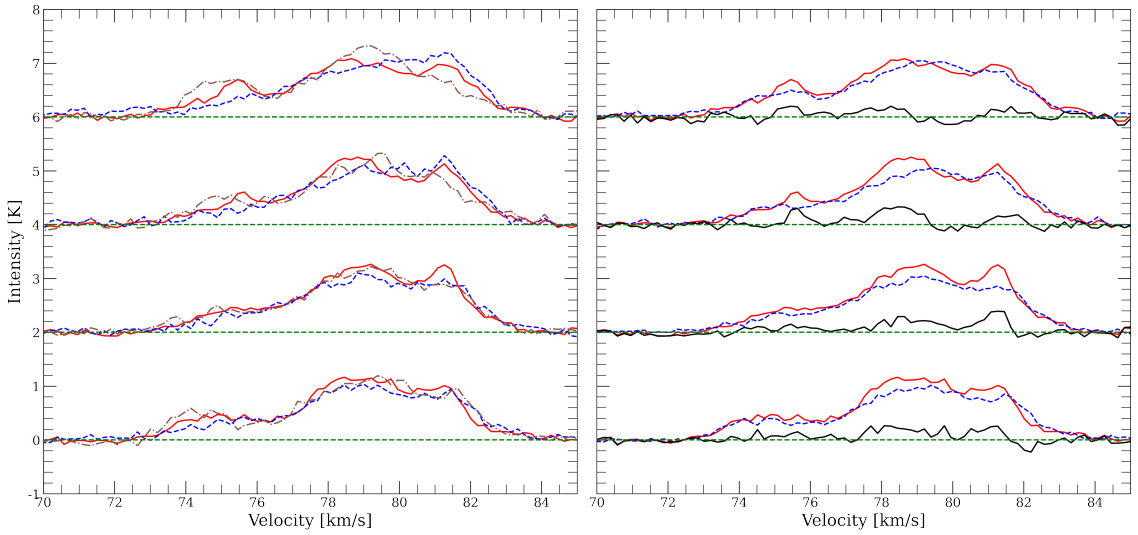

Figure 4.2: Same as Figure 4.1, but for strips 5-8 (bottom to top).

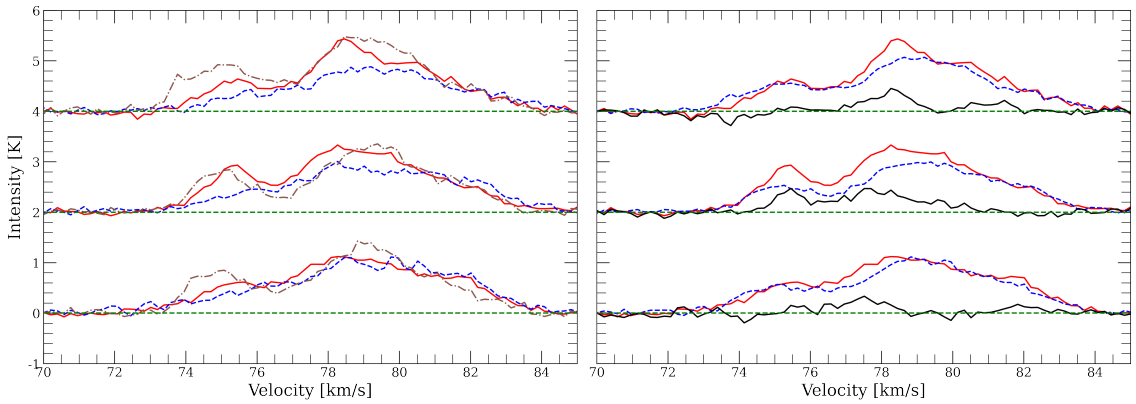

Figure 4.3: Same as Figure 4.1, but for strips 9-11 (bottom to top).

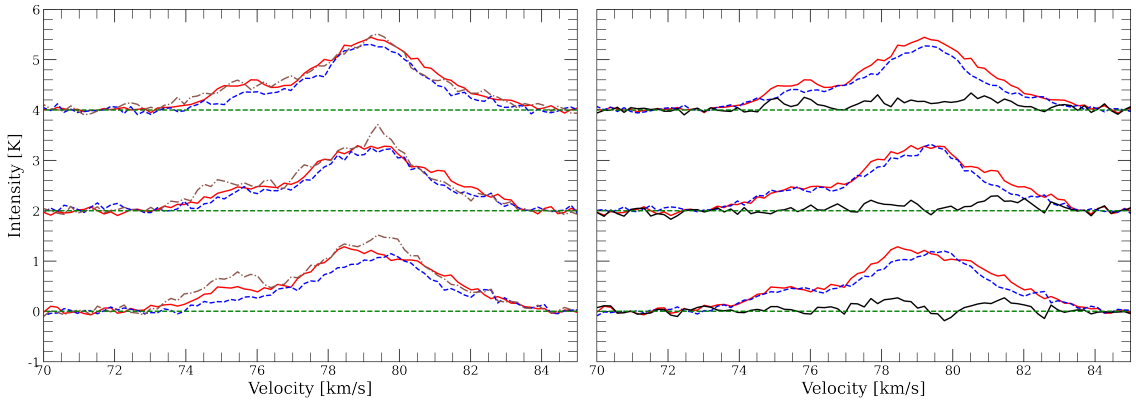

Figure 4.4: Same as Figure 4.1, but for strips 12-14 (bottom to top).

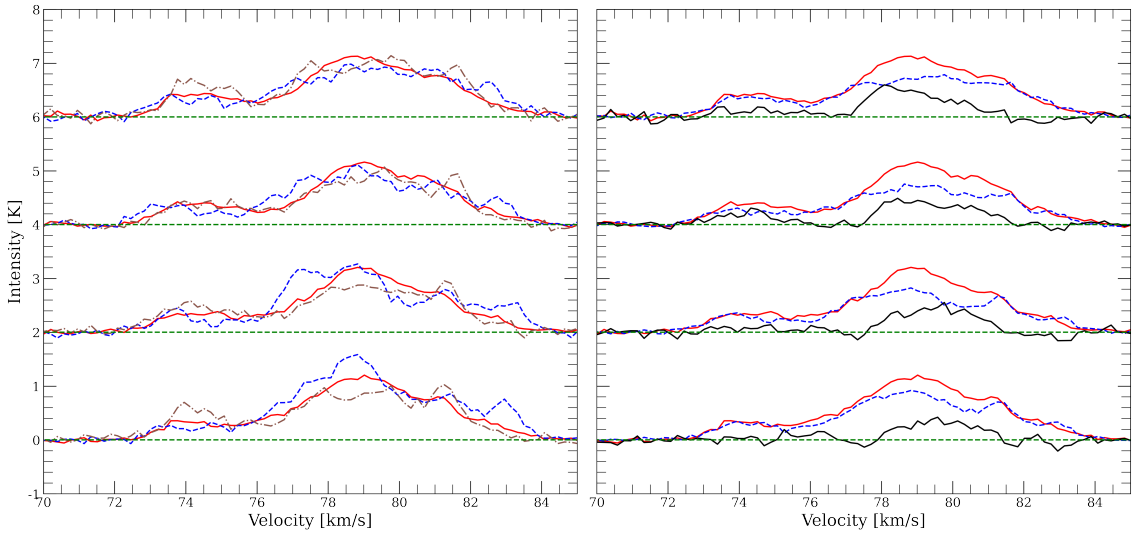

Figure 4.5: Same as Figure 4.1, but for for the outer strip regions.

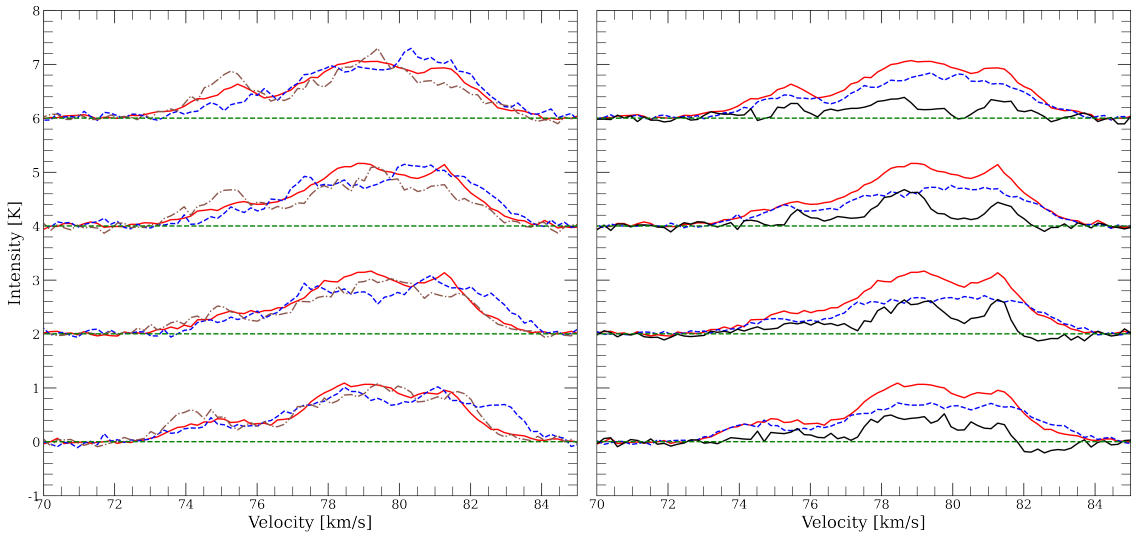

Figure 4.6: Same as Figure 4.5, but for strips 5-8 (bottom to top).

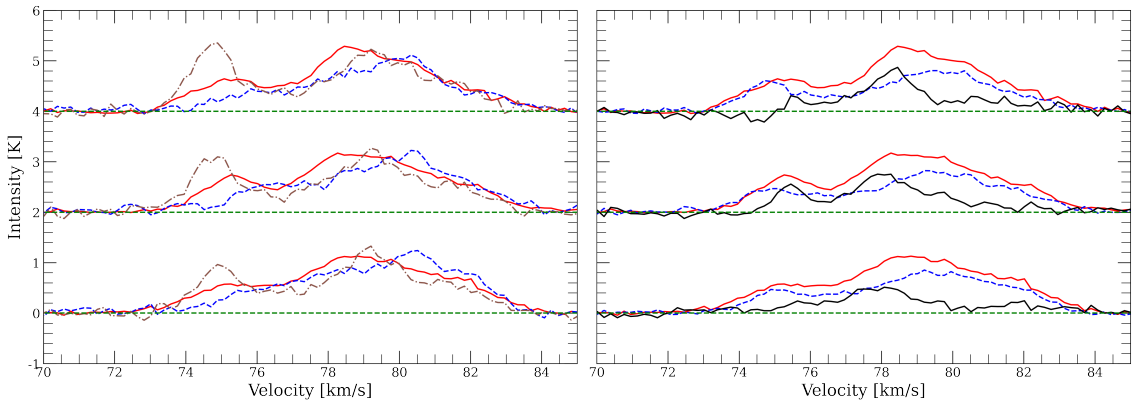

Figure 4.7: Same as Figure 4.5, but for strips 9-11 (bottom to top).

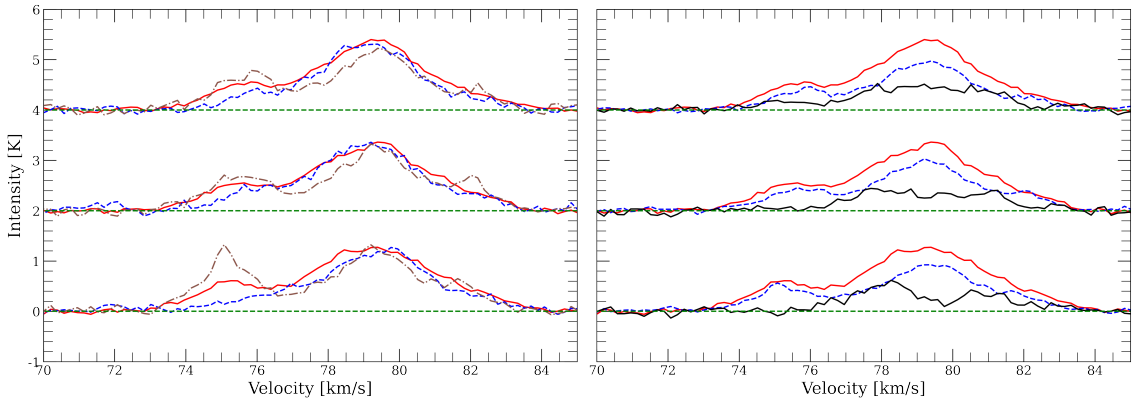

Figure 4.8: Same as Figure 4.5, but for strips 12-14 (bottom to top).

As described in Section 3.3.1, envelope subtraction was carried out. The results for this for the line masses and the virial line masses within the strips can be seen

in Figure 4.9. The left panels show the line mass of the filament regions, the middle panels show the virial line masses of the filaments, and the right panels show the ratio of the two. In the top row, the inner filament case is shown, while the bottom row shows the outer filament case. The different colors correspond to different cases of envelope subtraction: Blue is for no envelope subtraction, red is for masses envelope subtracted, and black is for both masses and spectra envelope subtracted. For the line masses, the decrease due to the envelope subtraction can be seen to be similar across all of the strips. This might indicate that the mass envelope is of similar importance all along the filament. The same can not be said about the virial line mass, however. In most cases it increases, following an increase in the computed velocity dispersions. However, in a few cases it decreases instead, due to a decrease in the computed velocity dispersions.

Another thing to note is that the envelope subtraction of the spectra seems to have a greater importance in the inner case compared to the outer case, as can be seen in the right panels of Figure 4.9. This might be due to the larger fraction of the envelope spectra being subtracted from the "on" region spectra in the inner compared to the outer case.

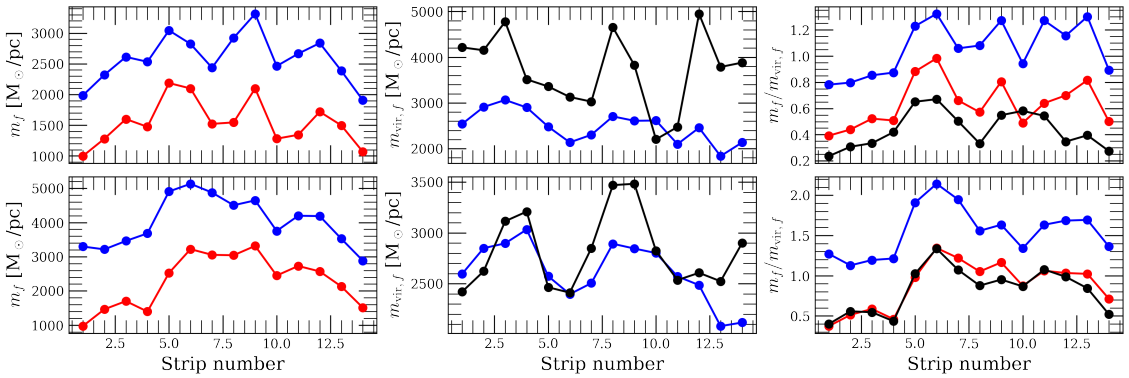

Figure 4.9: Comparison figures for the different cases of envelope subtraction for the filament line mass (m_f, left), virial line mass ($M_{\mathrm{vir},f}$, middle), and the ratio of the two (right). Top panels are for the inner filament case, while the bottom panels are for the outer filament case. The blue represents the no envelope subtraction case, the red is for masses envelope subtracted, and the black is for both masses and spectra envelope subtracted.

The filament and envelope kinetic pressures can be seen in Figure 4.10 (P_f and P_e, left and middle panels respectively), while the ratio P_e/P_f is seen in the right panels. Top and bottom rows, as well as the color scheme is the same as in Figure 4.9. The effect of the envelope subtraction of mass can be seen to be roughly the same as in Figure 4.9, which is to be expected as the kinetic pressure is directly proportional to the density, and thus the mass. The effect of also doing envelope subtraction of spectra can be seen to have a more varied effect. In some cases, the increase in velocity dispersion is large enough to balance the decrease in mass (see strips 3, 5, 6, 12 and 13 in the top left and top right panels of Figure 4.10). It can also be noted that the envelope to filament pressure ratio is less than one in most cases, only exceeding one in a few strips for the outer cases with envelope subtraction. The

main reason for the outer strip regions exceeding one here seems to be the envelope subtraction of mass, due to the similarity between the red and black lines.

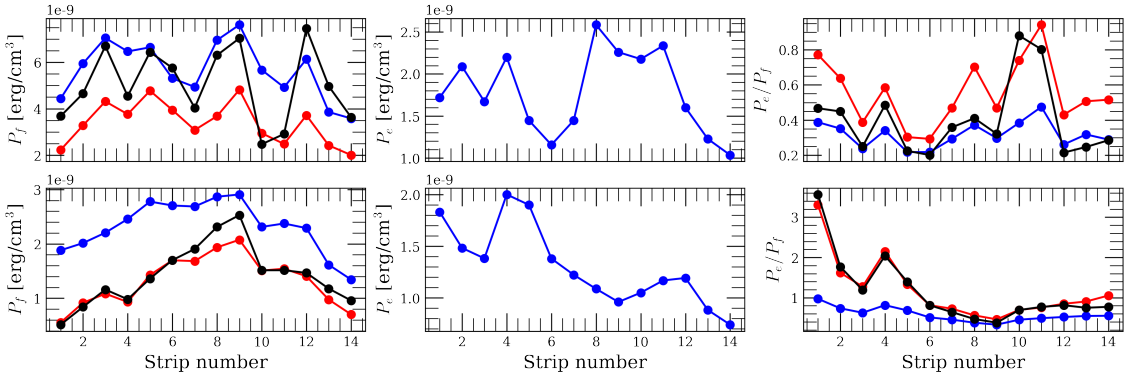

Figure 4.10: Comparison figures for the different cases of envelope subtraction for the filament pressure (P_f, left), envelope pressure (P_e, middle), and the ratio P_e/P_f (right). Top panels are for the inner filament case, while the bottom panels are for the outer filament case. The blue represents the no envelope subtraction case, the red is for masses envelope subtracted, and the black is for both masses and spectra envelope subtracted.

With the above presented results it is possible to compare to the model of filamentary virial equilibrium of Fiege & Pudritz (2000) presented in Section 2.1.2 (in particular Equation (2.5)). The results are presented in Figure 4.11. There, the envelope to filament pressure ratio is plotted against the ratio of the line mass to the virial line mass for the three different cases presented above. In all panels, the red dots represent the inner filament values, while the blue dots represent the outer filament values. The black lines show Equation (2.5) for different values of the magnetic to gravitational energy ratio (see values in the upper left panel), where the dashed line indicates magnetic neutrality. Also shown in the upper left panel is the typical estimated error.

It can be seen in Figure 4.11 that the inner filament would be generally consistent with magnetic neutrality for the cases without envelope subtraction and with masses envelope subtracted. In the case where spectra have been envelope subtracted as well, the inner filament case instead seems to be consistent with $\mathcal{M}/|\mathcal{W}| = -1$ instead, indicating that magnetic fields are needed to provide extra confinement for the filament to be in virial equilibrium. This can be compared to what Hernandez et al. (2012) found in the case of IRDC G35.30-0.33 (Cloud H, see their Figure 2). They only considered one case, which was with envelope subtraction of masses and spectra, for which they found the inner filament to have values consistent with the case of magnetically neutral virial equilibrium. It can also be noted that the pressure ratio generally increases as one zooms out from the inner to the outer filament, which is the same general behavior that Hernandez et al. (2012) found for their cloud. However, in contrast to their results, this study finds that the line mass ratio generally increases as one zooms out from the inner filament to the outer.

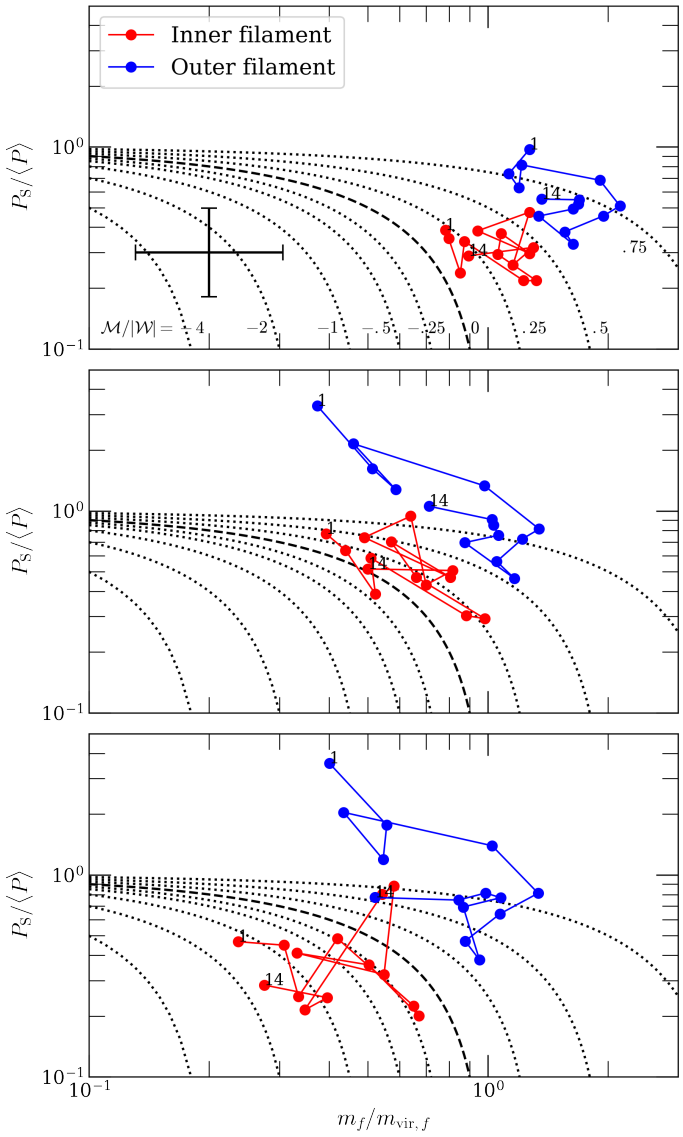

Figure 4.11: Ratio of envelope to filament pressure, P_e/P_f, against filament line mass ratio, $m_f/m_{\mathrm{vir},f}$. The top panel shows the case of no envelope subtraction. The middle panel shows the case where mass surface densities have been envelope subtracted. The bottom panel shows the case where mass surface densities and spectra have been envelope subtracted. The dashed and dotted lines correspond to different values of $\mathcal{M}/|\mathcal{W}|$ in Equation (2.5): The magnetically neutral case ($\mathcal{M}/|\mathcal{W}| = 0$, dashed), and magnetic confinement (< 0, dotted) and support (> 0, also dotted) (see top panel for exact values). The typical error of the quantities is also shown in the top left panel.

Moving on, the virial state of the different parts of the cloud are assessed. This is done by comparing the computed envelope to filament pressure ratio (left hand side of Equation (2.6)) to the right hand side of Equation (2.6). In order to make this comparison, estimates of the magnetic pressure terms are needed. Since this filamentary virial analysis mainly concerns radial stability of filaments, the analysis should only consider the magnetic field component which is able to provide radial

support/confinement. This component is the one along the filament (taken to be the east-west component here for simplicity). This component was computed from the plane of sky magnetic field map and the polarization angle ($\theta_{\rm pol}$) map as

$$B_{\rm along} = B_{\rm PoS} |\sin(\theta_{\rm pol})|,$$

where the polarization angle is measured from the north towards the east. The resulting map can be seen in the bottom right panel of Figure 3.4. It can be seen that the magnetic field strength varies along the filament. Notable are the low values within the inner filament regions of strips $\sim 4-10$, since many ALMA continuum sources have been found towards this region (see middle left panel of Figure 3.4). This part with low field strength along the filament and many continuum sources (strips 4-10) are termed the center region, while strips 1-3 are termed the east region, and strips 11-14 the west region.

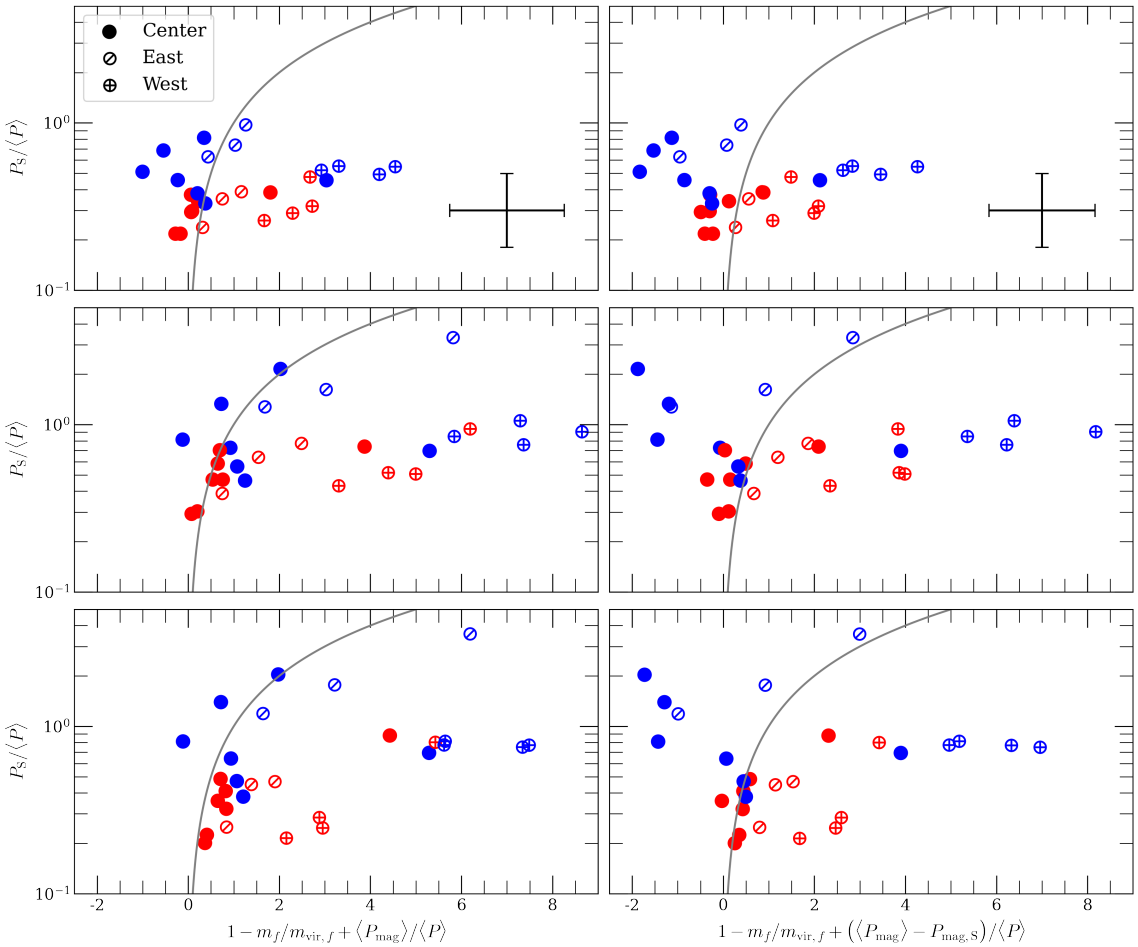

Figure 4.12: Comparisons of the left and right hand sides of Equation (2.6). The top row shows the case without envelope subtraction, the middle row the case with masses envelope subtracted, and the bottom row shows the case with masses and spectra envelope subtracted. The left column shows the case where the magnetic surface pressure has been neglected, while the right column considers it. The gray line is the virial (one-to-one) line. Red and blue points are for the inner and outer filament regions respectively.

From the computations of the magnetic pressures from the field strength map (bottom right panel of Figure 3.4), the virial state within the different strips can be assessed. The results can be seen in Figure 4.12, where the left and right hand sides of Equation (2.6) are compared with each other. It can be seen that the inner filament regions of the center region (marked as filled red dots) generally lie close to the one to one line (gray line). The other points for the inner filament are generally further from the one-to-one line, with the east region being generally somewhat closer. This could indicate that the regions where stars are forming are closer to virial equilibrium than other regions, and that these other regions generally have a large amount of magnetic pressure support against collapse.

4.2 Depletion analysis

As described in Section 3.4, in order to compute the $C^{18}O$ depletion factor two different measures of the column density of gas-phase $C^{18}O$ are needed. These are termed the observed column density, computed from the $C^{18}O$ spectral data, and the expected column density, computed from the Herschel mass surface density map and the the Spitzer extinction map. In the case of the Herschel map, the GBT $C^{18}O$ data was regridded to match the spatial resolution of the Herschel map. In the case of the extinction data, it was regridded to match the spatial resolution of the GBT data instead. For both of these cases, the range of integration for computing the observed column density was taken to be $70 - 85$ km/s, as that is the range over which $C^{18}O$ emission was seen (see Figures 4.1-4.8).

The resulting column density maps for the Herschel case can be seen in Figure 4.13. The left panel shows the observed column density, while the right panel shows the expected column density. The different color scales in the two panels should be noted, where the scale in the left panel only comprises the bottom ∼fifth of that of the right panel. Thus, it should be pointed out that the expected column density is, in general, higher than the observed one within the main filament of the cloud. It can also be noted that the shape of the cloud is more easily seen in the right panel of Figure 4.13 compared to the left panel. This can be explained by the $C^{18}O$ being more extended than the sub-mm emission used to derive the Herschel mass surface density map. Also worth to note is that the peak value of the expected column density for regions within the strips considered (see Figure 3.4) is $\sim 1.3 \cdot 10^{17}$ cm^{-2}.

For the case of the extinction map the resulting column densities can be seen in Figure 4.14 (observed column density in the left panel, and expected in the right panel). Comparing the left panel here to the left panel of Figure 4.13, most of the same general features can be seen, although less pronounced. Again, more detailed cloud structure can be seen in the expected column density map than the observed one. However, in this case the magnitude of the column densities are fairly similar across the main cloud filament, as opposed to in Figure 4.13.

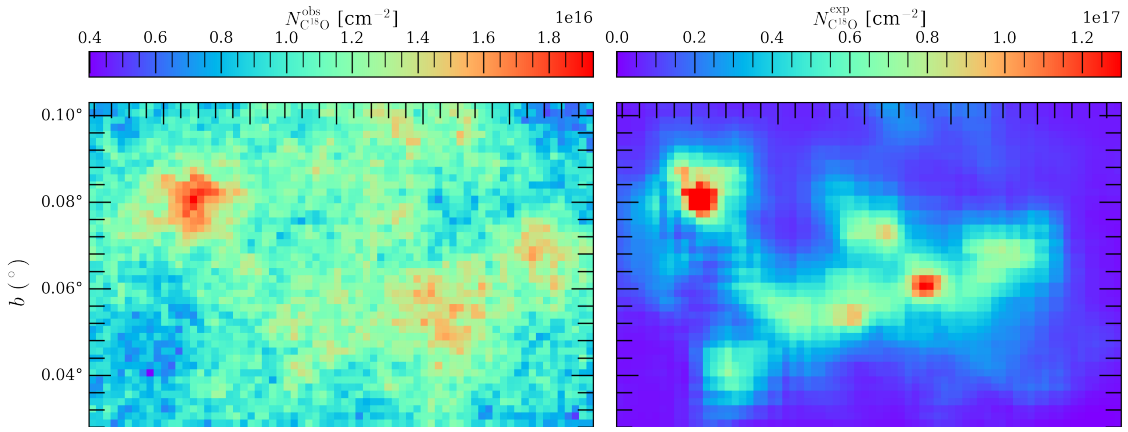

Figure 4.13: Left: Observed $C^{18}O$ column density (i.e. computed from the $C^{18}O$ data). The data has been regridded to match the spatial resolution of the Herschel mass surface density map. Right: Expected $C^{18}O$ column density computed from the Herschel column density map.

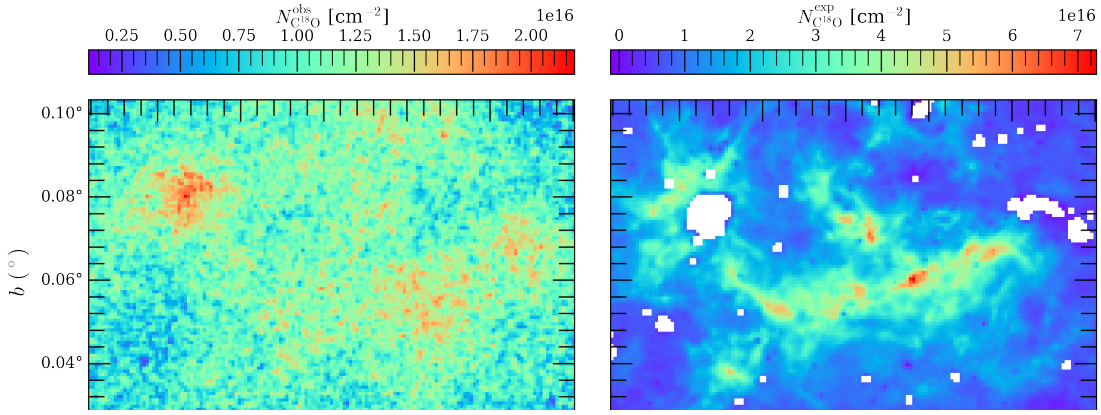

Figure 4.14: Left: Observed $C^{18}O$ column density (i.e. computed from the $C^{18}O$ data). Right: Expected $C^{18}O$ column density computed from the Spitzer extinction map regridded to match the spatial resolution of the GBT $C^{18}O$(1-0) data.

The depletion maps resulting from the the above column density maps (Figures 4.13 and 4.14) can be seen in Figure 4.15 for the Herschel mass surface density map case, and in Figure 4.16 for the case of the extinction map based calculations. In the left panel of Figure 4.15, the excitation temperature has been assumed to be 7.5 K everywhere, while in the right panel the excitation temperature is set to 20 K within the black box (the C9 region), but is kept at 7.5 K elsewhere. This was done to better match the derived dust temperature of that region (see Figure 3 of Lim et al., 2016). It should be noted that the color scale has been truncated at $f_D = 10$ in order to match the peak value outside the C9 region, while the depletion can be seen to be higher in the C9 region. Due to the higher temperature, the lower energy levels will be less populated as the molecules can be more readily excited. This might be a reason behind the higher depletion factors towards the C9 region, in contrast to the more established view of depletion being due to freeze out onto

dust grains.

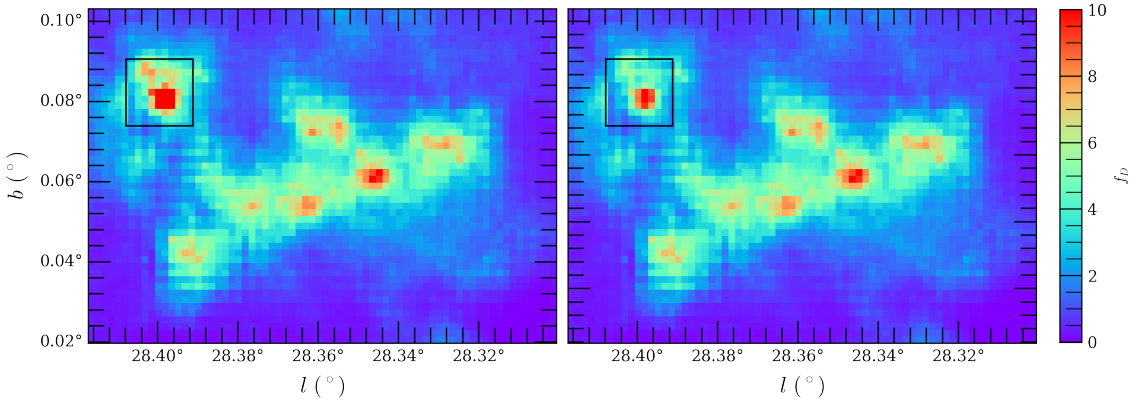

Figure 4.15: Left: Depletion map derived from the Herschel mass surface density map and the GBT $C^{18}O$ data, assuming $T_{ex} = 7.5$ K. Right: Same as on the left, but assuming $T_{ex} = 20$ K towards the C9 region (marked by the black box in both panels). The color scale has been truncated at 10 to match the peak value of the depletion factor outside of the C9 region.

The extinction map derived depletion map is shown in Figure 4.16. Again the excitation temperature was assumed to be 7.5 K everywhere. Due to there already being a hole in the extinction map towards the C9 region, caused by a MIR-bright source at that location, there is no need to change the excitation temperature in this case. Comparing this map to the ones in Figure 4.15 it can be seen that the depletion is generally lower in this case. This mainly stems from the decrease in the column density map derived from the extinction map compared to the one from the mass surface density map.

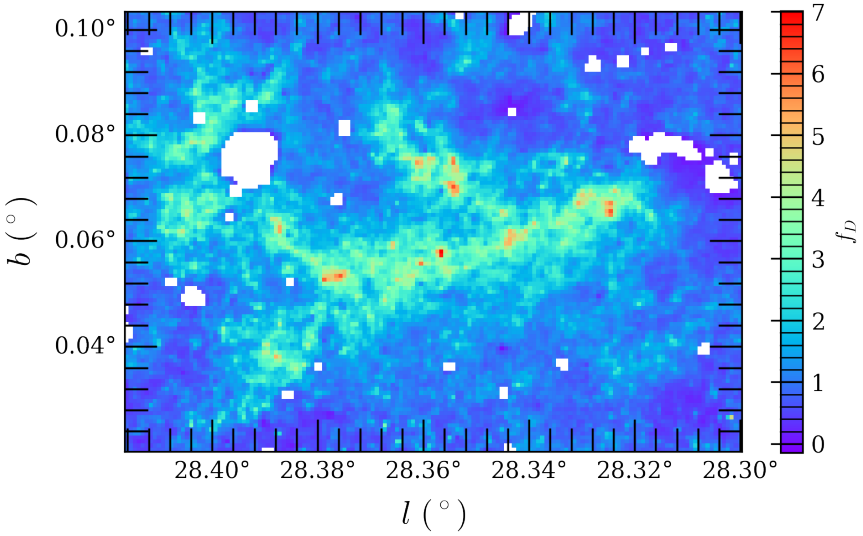

Figure 4.16: Depletion map derived from the Spitzer extinction map and the GBT $C^{18}O$ data, assuming $T_{ex} = 7.5$ K.

5

Discussion & Conclusions

In this chapter the results presented in Chapter 4 are put in context of the different theories of massive star formation, as well as compared to results found in previous studies. The general conclusions of this work are also summarized.

5.1 The virial state of G28.37+0.07

The dynamical state of the cloud has strong implications on different theories of massive star formation. Theories such as the core accretion model suggest that the formation of massive stars and star clusters occur in an equilibrium state. On the other hand, competitive accretion (or hierarchical gravitational collapse) suggests clouds to be always supercritical. From Figure 4.12 it is found that the virial state varies along the filament, with what we call the center region being closer, in general, to virial equilibrium than the east and west ends. As this also is the region where most of the ALMA continuum sources are found, these general results favor massive star formation occurring at equilibrium conditions (McKee & Tan, 2003; Tan et al., 2013). The need to include surface terms in the virial analysis should also be stressed, as neglecting this may overestimate the contribution of the magnetic field support. The most striking feature against some literature studies on the same region (e.g. Liu et al., 2024) is that the cloud goes from supercritical (i.e. gravity dominated) to equilibrium or even slightly subcritical instead of going from subcritical to super critical with column density. This difference probably arises by properly taking the cloud geometry into account and also including the surface pressure terms.

5.2 $C^{18}O$ depletion

As mentioned in Section 1.3.1, Entekhabi et al. (2022) computed abundances for several different molecules towards ten regions of cloud C. These regions can be seen in Figure 5.1, overlaid on the depletion map of the left panel of Figure 4.15. Since one of the molecules studied was $C^{18}O$, depletion factors can be computed from their abundances and compared to what is found in this work.

The depletion factor was computed towards the ten regions by extracting average spectra to compute the observed column density of $C^{18}O$. Firstly, the velocity range $70-85$ km/s was used, matching what was used to construct the depletion maps. The results of these calculations can be seen compared to the depletion factors computed from the abundances of Entekhabi et al. (2022) in the left panel of Figure 5.2. It can be seen that the depletion factors from this work (f_D(L)) are, in general, slightly

higher than those of Entekhabi et al. (2022) (f_D(E)), with values ranging between $\sim$ 5 and 13. However, Entekhabi et al. (2022) used the range $77 - 82$ km/s in their abundance calculations. Thus, in order to get a more fair comparison, the depletion factors were computed using this velocity range as well. The effect of this was increasing the depletion factors further to $\sim 8 - 20$, now always being higher than those of Entekhabi et al. (2022). An explanation for this difference might be that different telescopes were used for the $C^{18}O$ observations, with this work using GBT, while Entekhabi et al. (2022) used IRAM. One should note that some of the values of f_D towards these ten regions are larger than any of the values found within the depletion maps. This shows that the order in which averaging is done, that is using average spectra and mass surface density versus averaging already computed depletion factors, can have a large impact on the results.

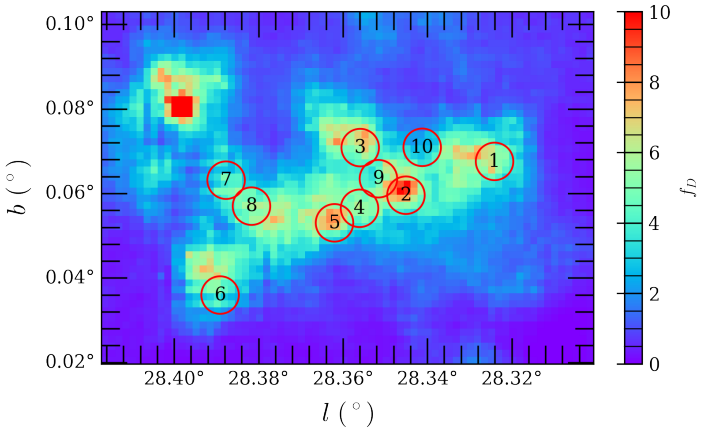

Figure 5.1: Ten regions studied by Entekhabi et al. (2022) (red circles) overlaid on the depletion map of the left panel of Figure 4.15.

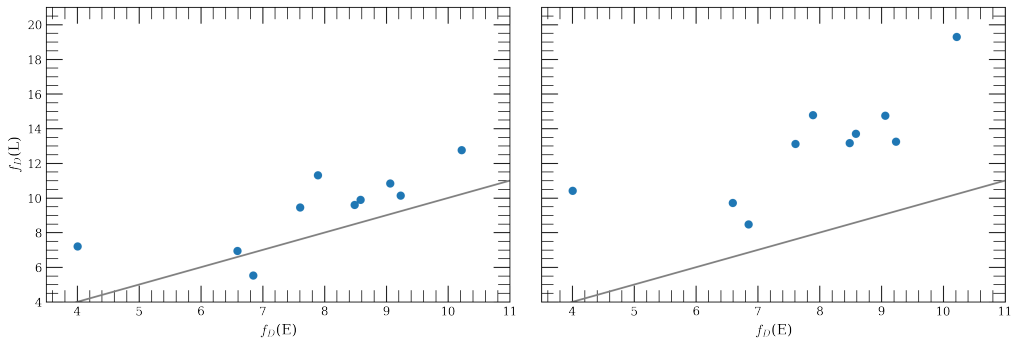

Figure 5.2: Comparisons between the depletion factors derived in this work ($f_D(L)$) and those derived from the abundances of Entekhabi et al. (2022) ($f_D(E)$). The left panel has f_D(L) computed from the velocity range $70 - 85$ km/s, while in the right panel it is instead computed from the range $77 - 82$ km/s, matching the range used in Entekhabi et al. (2022).

5.3 Conclusions and future outlooks

In this work, a filamentary virial analysis following Fiege & Pudritz (2000) has been conducted, including contributions from magnetic fields and surface terms, along the main filament of IRDC G28.37+0.07. The main findings of this analysis are as follows: The virial state of the cloud seems to change from supercritical to close to equilibrium from the outer to the inner filament, which seems to be in opposition to what has been found in previous studies. Magnetic fields are dynamically important in setting the initial conditions for massive star and star cluster formation. It is important to take surface terms into account when assessing the virial state of these kinds of structures. These overall findings might point slightly towards massive star formation occurring in equilibrium conditions.

Also as a part of this work, the state of $C^{18}O$ depletion was studied. The results of the depletion maps point towards $C^{18}O$ being highly depleted across the cloud, with depletion factors generally > 3, and with values upwards of 10 in certain regions. Comparisons were also made for ten regions studied by Entekhabi et al. (2022). This work generally finds higher values of the depletion factor than Entekhabi et al. (2022), possibly stemming from different telescope being used to observe the molecular line emission. All of these results point towards $C^{18}O$ being highly depleted, and this should be taken into account when conducting further studies.

In order to get an even better understanding of the importance of magnetic fields in the process of massive star formation, similar analysis to what gthas been done in this work is planned for more clouds in the POLIMAP survey. Among these are Clouds F and H, which, as mentioned previously, have been studied by Hernandez et al. (2011a) and Hernandez et al. (2012). With the inclusion of magnetic terms, it will be interesting to see how the results will differ from those previously obtained.

Bibliography

André, P., Di Francesco, J., Ward-Thompson, D., et al. 2014, in Protostars and Planets VI, ed. H. Beuther, R. S. Klessen, C. P. Dullemond, & T. Henning, 27–51

Barnes, A. T., Liu, J., Zhang, Q., et al. 2023, A&A, 675, A53, doi: 10.1051/0004-6361/202245668

Bonnell, I. A., Bate, M. R., Clarke, C. J., & Pringle, J. E. 1997, MNRAS, 285, 201, doi: 10.1093/mnras/285.1.201

—. 2001, MNRAS, 323, 785, doi: 10.1046/j.1365-8711.2001.04270.x

Bradley, L., Deil, C., Patra, S., et al. 2022, astropy/regions:, v0.5, Zenodo, doi: 10.5281/zenodo.5826359. https://doi.org/10.5281/zenodo.5826359

Butler, M. J., & Tan, J. C. 2009, The Astrophysical Journal, 696, 484, doi: 10.1088/0004-637X/696/1/484

—. 2012, The Astrophysical Journal, 754, 5, doi: 10.1088/0004-637X/754/1/5

Butler, M. J., Tan, J. C., & Kainulainen, J. 2014, ApJ, 782, L30, doi: 10.1088/2041-8205/782/2/L30

Caselli, P., Walmsley, C. M., Tafalla, M., Dore, L., & Myers, P. C. 1999, ApJ, 523, L165, doi: 10.1086/312280

Draine, B. T. 2011, Physics of the Interstellar and Intergalactic Medium

Entekhabi, N., Tan, J. C., Cosentino, G., et al. 2022, A&A, 662, A39, doi: 10.1051/0004-6361/202142601

Falgarone, E., Pety, J., & Phillips, T. G. 2001, The Astrophysical Journal, 555, 178, doi: 10.1086/321483

Fiege, J. D., & Pudritz, R. E. 2000, MNRAS, 311, 85, doi: 10.1046/j.1365-8711.2000.03066.x

Goldsmith, P. F., & Langer, W. D. 1978, ApJ, 222, 881, doi: 10.1086/156206

Hacar, A., Clark, S. E., Heitsch, F., et al. 2023, in Astronomical Society of the Pacific Conference Series, Vol. 534, Protostars and Planets VII, ed. S. Inutsuka, Y. Aikawa, T. Muto, K. Tomida, & M. Tamura, 153

Harper, D. A., Runyan, M. C., Dowell, C. D., et al. 2018, Journal of Astronomical Instrumentation, 07, 1840008, doi: 10.1142/S2251171718400081

Hernandez, A. K., & Tan, J. C. 2015, ApJ, 809, 154, doi: 10.1088/0004-637X/809/2/154

Hernandez, A. K., Tan, J. C., Caselli, P., et al. 2011a, ApJ, 738, 11, doi: 10.1088/0004-637X/738/1/11

—. 2011b, ApJ, 738, 11, doi: 10.1088/0004-637X/738/1/11

Hernandez, A. K., Tan, J. C., Kainulainen, J., et al. 2012, ApJ, 756, L13, doi: 10.1088/2041-8205/756/1/L13

Kainulainen, J., & Tan, J. C. 2013, A&A, 549, A53, doi: 10.1051/0004-6361/201219526

Kong, S. 2019, ApJ, 873, 31, doi: 10.3847/1538-4357/aaffd5

Kong, S., Arce, H. G., Maureira, M. J., et al. 2019a, ApJ, 874, 104, doi: 10.3847/1538-4357/ab07b9

—. 2019b, ApJ, 874, 104, doi: 10.3847/1538-4357/ab07b9

Kong, S., Tan, J. C., Arce, H. G., et al. 2018, ApJ, 855, L25, doi: 10.3847/2041-8213/aab151

Krumholz, M. R. 2015, Notes on Star Formation (arXiv e-prints), arXiv:1511.03457, doi: 10.48550/arXiv.1511.03457

Lamers, H. J. G. L. M., & Levesque, E. M. 2017, Understanding Stellar Evolution, doi: 10.1088/978-0-7503-1278-3

Law, C.-Y., Tan, J. C., Skalidis, R., et al. 2024, arXiv e-prints, arXiv:2401.11560, doi: 10.48550/arXiv.2401.11560

Lim, W., Tan, J. C., Kainulainen, J., Ma, B., & Butler, M. J. 2016, The Astrophysical Journal Letters, 829, L19, doi: 10.3847/2041-8205/829/1/L19

Liu, J., Zhang, Q., Lin, Y., et al. 2024, ApJ, 966, 120, doi: 10.3847/1538-4357/ad3105

Mangum, J. G., & Shirley, Y. L. 2015, PASP, 127, 266, doi: 10.1086/680323

McClure-Griffiths, N. M., Dickey, J. M., Gaensler, B. M., Green, A. J., & Haverkorn, M. 2006, The Astrophysical Journal, 652, 1339, doi: 10.1086/508706

McKee, C. F., & Tan, J. C. 2003, ApJ, 585, 850, doi: 10.1086/346149

Moser, E., Liu, M., Tan, J. C., et al. 2020, ApJ, 897, 136, doi: 10.3847/1538-4357/ab96c1

Müller, H. S. P., Schlöder, F., Stutzki, J., & Winnewisser, G. 2005, Journal of Molecular Structure, 742, 215, doi: 10.1016/j.molstruc.2005.01.027

Pattle, K., Fissel, L., Tahani, M., Liu, T., & Ntormousi, E. 2023, in Astronomical Society of the Pacific Conference Series, Vol. 534, Protostars and Planets VII, ed. S. Inutsuka, Y. Aikawa, T. Muto, K. Tomida, & M. Tamura, 193

Rathborne, J. M., Jackson, J. M., & Simon, R. 2006, ApJ, 641, 389, doi: 10.1086/500423

Schneider, S., & Elmegreen, B. G. 1979, ApJS, 41, 87, doi: 10.1086/190609

Shu, F. H., Adams, F. C., & Lizano, S. 1987, ARA&A, 25, 23, doi: 10.1146/annurev.aa.25.090187.000323

Sieth, M., Devaraj, K., Voll, P., et al. 2014, in Society of Photo-Optical Instrumentation Engineers (SPIE) Conference Series, Vol. 9153, Millimeter, Submillimeter, and Far-Infrared Detectors and Instrumentation for Astronomy VII, ed. W. S. Holland & J. Zmuidzinas, 91530P

Simon, R., Jackson, J. M., Rathborne, J. M., & Chambers, E. T. 2006a, ApJ, 639, 227, doi: 10.1086/499342

Simon, R., Rathborne, J. M., Shah, R. Y., Jackson, J. M., & Chambers, E. T. 2006b, ApJ, 653, 1325, doi: 10.1086/508915

Tan, J. C., Beltrán, M. T., Caselli, P., et al. 2014, in Protostars and Planets VI, ed. H. Beuther, R. S. Klessen, C. P. Dullemond, & T. Henning, 149–172

Tan, J. C., Kong, S., Butler, M. J., Caselli, P., & Fontani, F. 2013, ApJ, 779, 96, doi: 10.1088/0004-637X/779/2/96

A

Additional table and figures

Table A.1 summarizes all the quantities for the filamentary virial analysis.

Table A.1: Values for the different quantities. The first row for each quantity is without envelope subtraction, while second and third rows show envelope subtracted quantities (Without brackets: only Σ subtracted. With brackets: spectra also subtracted.). For the magnetic energies per unit length, the first and second rows are without and with the surface term respectively. The last column shows a total (either sum or mean) of the 14 strips.

Inner filament															
Cloud property	1_i	2_i	3_i	4_i	5_i	6_i	7_i	8_i	9_i	10_i	11_i	12_i	13_i	14_i	T_i
Σ_c(N) (g/cm^2)	0.1784	0.1619	0.1784	0.2053	0.3125	0.427	0.5504	0.2781	0.2169	0.2168	0.1977	0.1574	0.1143	0.1266	0.237
Σ_c(S) (g/cm^2)	0.3122	0.2141	0.1875	0.1773	0.1549	0.131	0.1652	0.2483	0.2225	0.2106	0.2796	0.2468	0.207	0.1763	0.21
$\Sigma_{\rm on}$ (g/cm^2)	0.3291	0.3847	0.4333	0.4201	0.5048	0.4683	0.404	0.4843	0.5497	0.4085	0.4419	0.4706	0.3958	0.3161	0.429
Σ_c (g/cm^2)	0.1711	0.1803	0.1755	0.1835	0.1485	0.1256	0.1584	0.2381	0.2107	0.205	0.2289	0.1938	0.1541	0.1453	0.18
Σ_f (g/cm^2)	0.3291	0.3847	0.4333	0.4201	0.5048	0.4683	0.404	0.4843	0.5497	0.4085	0.4419	0.4706	0.3958	0.3161	0.4294
	0.1653	0.2121	0.2653	0.2444	0.3626	0.348	0.2523	0.2563	0.348	0.2123	0.2228	0.2851	0.2483	0.177	0.257
M_c ($M_\odot$)	1040	1096	1066	1115	902.8	763.6	962.9	1447	1281	1246	1391	1178	936.4	882.9	1.531e+4
M_f ($M_\odot$)	1000	1169	1317	1276	1534	1423	1228	1472	1670	1241	1343	1430	1203	960.5	1.827e+4
	502.2	644.6	806.2	742.7	1102	1058	766.8	779	1058	645.3	677	866.3	754.6	538	1.094e+4
m_f ($M_\odot$/pc)	1985	2320	2613	2533	3045	2824	2437	2921	3316	2464	2665	2838	2387	1907	2590
	996.8	1279	1600	1474	2187	2099	1522	1546	2099	1281	1344	1719	1498	1068	1551
$m_{\rm vir,f}$ ($M_\odot$/pc)	2539	2911	3064	2900	2480	2136	2302	2705	2609	2615	2098	2457	1836	2135	2485
	[4215]	[4152]	[4776]	[3515]	[3359]	[3129]	[3028]	[4654]	[3824]	[2203]	[2474]	[4950]	[3787]	[3882]	[3711]
v_f (km/s)	78.7	78.53	78.4	78.44	78.75	78.98	78.88	78.71	78.67	78.5	78.84	78.73	78.91	78.79	78.7
	[78.31]	[78.47]	[77.09]	[77.9]	[78.4]	[78.89]	[78.11]	[78.08]	[78.09]	[77.5]	[78.85]	[78.18]	[79.64]	[78.76]	[78.31]
v_c (km/s)	78.63	78.44	78.66	78.45	78.85	78.89	78.98	78.7	78.55	78.75	78.53	78.79	78.57	78.75	78.68
σ_f (km/s)	2.342	2.507	2.573	2.503	2.314	2.148	2.23	2.417	2.374	2.377	2.129	2.303	1.991	2.147	2.311
	[3.011]	[2.988]	[3.205]	[2.749]	[2.688]	[2.594]	[2.552]	[3.164]	[2.868]	[2.176]	[2.306]	[3.263]	[2.854]	[2.889]	[2.808]
σ_c (km/s)	2.476	2.659	2.411	2.705	2.437	2.369	2.361	2.574	2.558	2.546	2.496	2.245	2.204	2.085	2.438
ρ_f ($M_\odot$/pc^3)	1195	1397	1573	1525	1833	1700	1467	1758	1996	1483	1604	1709	1437	1148	1559
	600	770.2	963.1	887.3	1317	1263	916.1	930.6	1263	770.9	808.9	1035	901.5	642.7	933.6
ρ_c ($M_\odot$/pc^3)	414.2	436.4	424.7	444.1	359.5	304.1	383.5	576.4	510.1	496.1	554	469.2	372.9	351.6	435.5
$\langle P \rangle$ (erg/cm^3)	4.435e-9	5.944e-9	7.045e-9	6.465e-9	6.643e-9	5.309e-9	4.936e-9	6.952e-9	7.611e-9	5.669e-9	4.921e-9	6.136e-9	3.857e-9	3.581e-9	5.679e-9
	2.227e-9	3.277e-9	4.314e-9	3.762e-9	4.772e-9	3.946e-9	3.083e-9	3.68e-9	4.818e-9	2.947e-9	2.481e-9	3.717e-9	2.42e-9	2.006e-9	3.389e-9
	[3.681e-9]	[4.654e-9]	[6.695e-9]	[4.539e-9]	[6.437e-9]	[5.754e-9]	[4.037e-9]	[6.304e-9]	[7.032e-9]	[2.471e-9]	[2.912e-9]	[7.457e-9]	[4.969e-9]	[3.631e-9]	[5.041e-9]
$P_{\rm S}$ (erg/cm^3)	1.719e-9	2.089e-9	1.671e-9	2.2e-9	1.445e-9	1.155e-9	1.447e-9	2.585e-9	2.26e-9	2.177e-9	2.337e-9	1.6e-9	1.226e-9	1.034e-9	1.782e-9
B_f (mG)	0.7488	0.7835	0.7966	0.8184	0.7401	0.6494	0.6043	0.6144	0.6435	0.8336	0.9689	1.042	1.214	1.005	0.8241
B_f^2 (mG^2)	0.5821	0.6346	0.6649	0.7185	0.568	0.4388	0.3723	0.3808	0.4271	0.719	0.9985	1.125	1.516	1.063	0.7404
$\mathcal{W}$ (erg/cm)	-1.092e+29	-1.492e+29	-1.892e+29	-1.779e+29	-2.57e+29	-2.211e+29	-1.645e+29	-2.365e+29	-3.047e+29	-1.683e+29	-1.969e+29	-2.233e+29	-1.58e+29	-1.007e+29	-1.897e+29
	-2.754e+28	-4.537e+28	-7.096e+28	-6.022e+28	-1.326e+29	-1.221e+29	-6.419e+28	-6.625e+28	-1.221e+29	-4.546e+28	-5.005e+28	-8.193e+28	-6.217e+28	-3.16e+28	-7.018e+28
$\mathcal{M}$ (erg/cm)	1.317e+29	1.008e+29	3.539e+28	1.866e+28	1.259e+28	7.18e+27	1.943e+28	3.11e+28	8.597e+28	3.135e+29	4.57e+29	3.523e+29	3.676e+29	2.465e+29	1.557e+29
	8.777e+28	6.512e+28	2.502e+28	2.692e+25	2.97e+26	-1.378e+28	-6.741e+28	-4.563e+28	-6.266e+27	1.476e+29	2.721e+29	2.392e+29	2.903e+29	2.128e+29	8.622e+28
Outer filament															
Cloud property	1_o	2_o	3_o	4_o	5_o	6_o	7_o	8_o	9_o	10_o	11_o	12_o	13_o	14_o	T_o
Σ_c(N) (g/cm^2)	0.1845	0.09919	0.1061	0.2078	0.2758	0.2321	0.2048	0.126	0.09809	0.08054	0.08511	0.09922	0.08458	0.09278	0.141
Σ_c(S) (g/cm^2)	0.3158	0.1786	0.1729	0.1547	0.102	0.07096	0.08399	0.1059	0.113	0.1263	0.1478	0.1573	0.1367	0.1252	0.142
$\Sigma_{\rm on}$ (g/cm^2)	0.2734	0.2665	0.287	0.3053	0.4069	0.4256	0.4043	0.3736	0.3853	0.3112	0.3481	0.3472	0.2923	0.2391	0.333
Σ_c (g/cm^2)	0.1873	0.1411	0.1417	0.184	0.1918	0.1539	0.1466	0.1178	0.1072	0.105	0.1183	0.1302	0.1123	0.1107	0.139
Σ_f (g/cm^2)	0.2734	0.2665	0.287	0.3053	0.4069	0.4256	0.4043	0.3736	0.3853	0.3112	0.3481	0.3472	0.2923	0.2391	0.3333
	0.08039	0.1212	0.141	0.1157	0.2092	0.267	0.2532	0.2522	0.2749	0.203	0.2262	0.213	0.1765	0.1251	0.19
M_c ($M_\odot$)	1708	1286	1291	1678	1749	1403	1337	1074	976.9	957.3	1078	1187	1024	1009	1.776e+4
M_f ($M_\odot$)	1662	1620	1744	1855	2473	2587	2457	2270	2342	1891	2116	2110	1776	1453	2.836e+4
	488.6	736.4	856.9	702.9	1272	1623	1539	1533	1671	1234	1375	1294	1073	760.3	1.616e+4
m_f ($M_\odot$/pc)	3298	3215	3462	3683	4908	5134	4877	4506	4648	3754	4199	4188	3526	2884	4020
	969.7	1462	1701	1395	2524	3221	3055	3043	3316	2449	2729	2569	2130	1509	2291
$m_{\rm vir,f}$ ($M_\odot$/pc)	2595	2849	2897	3033	2573	2396	2505	2892	2845	2801	2571	2486	2082	2117	2617
	[2420]	[2622]	[3115]	[3209]	[2464]	[2411]	[2849]	[3470]	[3483]	[2824]	[2535]	[2606]	[2523]	[2900]	[2816]
v_f (km/s)	78.73	78.6	78.63	78.57	78.86	78.99	78.95	78.68	78.62	78.63	78.59	78.68	78.67	78.77	78.71
	[78.81]	[78.74]	[78.67]	[78.26]	[78.54]	[78.72]	[78.72]	[78.34]	[78.36]	[78.49]	[78.55]	[78.85]	[78.49]	[78.69]	[78.59]
v_c (km/s)	78.67	78.53	78.55	78.59	79.03	79.1	78.99	78.81	78.67	78.57	78.47	78.46	78.7	78.75	78.71
σ_f (km/s)	2.368	2.481	2.501	2.559	2.357	2.275	2.326	2.499	2.479	2.46	2.357	2.317	2.121	2.138	2.374
	[2.281]	[2.374]	[2.588]	[2.627]	[2.302]	[2.277]	[2.475]	[2.732]	[2.737]	[2.464]	[2.335]	[2.367]	[2.329]	[2.497]	[2.456]
σ_c (km/s)	2.576	2.671	2.573	2.716	2.592	2.467	2.379	2.503	2.466	2.605	2.589	2.493	2.309	2.131	2.505
ρ_f ($M_\odot$/pc^3)	496.3	483.8	520.9	554.2	738.6	772.6	733.9	678.1	699.4	564.9	631.9	630.2	530.6	434	605
	145.9	220	255.9	209.9	379.8	484.7	459.7	457.9	499	368.5	410.7	386.6	320.5	227.1	344.7
ρ_c ($M_\odot$/pc^3)	408.1	307.3	308.6	400.9	417.9	335.2	319.4	256.5	233.4	228.7	257.7	283.7	244.7	241	303.1
$\langle P \rangle$ (erg/cm^3)	1.883e-9	2.015e-9	2.206e-9	2.457e-9	2.778e-9	2.706e-9	2.687e-9	2.867e-9	2.909e-9	2.313e-9	2.375e-9	2.29e-9	1.615e-9	1.343e-9	2.317e-9
	5.537e-10	9.161e-10	1.084e-9	9.307e-10	1.428e-9	1.698e-9	1.683e-9	1.936e-9	2.076e-9	1.509e-9	1.544e-9	1.405e-9	9.753e-10	7.029e-10	1.317e-9
	[5.139e-10]	[8.393e-10]	[1.16e-9]	[9.806e-10]	[1.362e-9]	[1.701e-9]	[1.906e-9]	[2.312e-9]	[2.53e-9]	[1.515e-9]	[1.515e-9]	[1.467e-9]	[1.177e-9]	[9.583e-10]	[1.424e-9]
$P_{\rm S}$ (erg/cm^3)	1.832e-9	1.484e-9	1.383e-9	2.001e-9	1.9e-9	1.381e-9	1.223e-9	1.088e-9	9.605e-10	1.051e-9	1.169e-9	1.193e-9	8.834e-10	7.409e-10	1.306e-9
B_f (mG)	0.606	0.595	0.5911	0.6443	0.6043	0.5589	0.5593	0.5719	0.5687	0.6637	0.766	0.8012	0.8796	0.7263	0.6562
B_f^2 (mG^2)	0.4139	0.4133	0.4163	0.4863	0.3982	0.3354	0.327	0.3332	0.3399	0.4927	0.676	0.7419	0.9478	0.6467	0.5042
$\mathcal{W}$ (erg/cm)	-3.015e+29	-2.864e+29	-3.321e+29	-3.759e+29	-6.677e+29	-7.305e+29	-6.591e+29	-5.628e+29	-5.988e+29	-3.905e+29	-4.887e+29	-4.861e+29	-3.446e+29	-2.306e+29	-4.611e+29
	-2.606e+28	-5.921e+28	-8.017e+28	-5.394e+28	-1.765e+29	-2.876e+29	-2.586e+29	-2.566e+29	-3.048e+29	-1.662e+29	-2.064e+29	-1.829e+29	-1.257e+29	-6.311e+28	-1.606e+29
$\mathcal{M}$ (erg/cm)	3.63e+29	2.935e+29	1.73e+29	1.752e+29	1.281e+29	4.786e+28	2.441e+29	2.765e+29	3.716e+29	9.884e+29	1.449e+30	1.043e+30	1.069e+30	6.221e+29	5.174e+29
	1.548e+29	4.936e+28	-2.143e+29	-2.846e+29	-2.188e+29	-2.364e+29	3.219e+28	9.389e+28	1.432e+29	7.215e+29	1.226e+30	9.572e+29	1.011e+30	5.42e+29	2.841e+29

Figures A.1, A.2, and A.3 show the three remaining continuum peaks considered in the radial profile offset analysis. Layout of the panels is the same as in Figure 3.3.

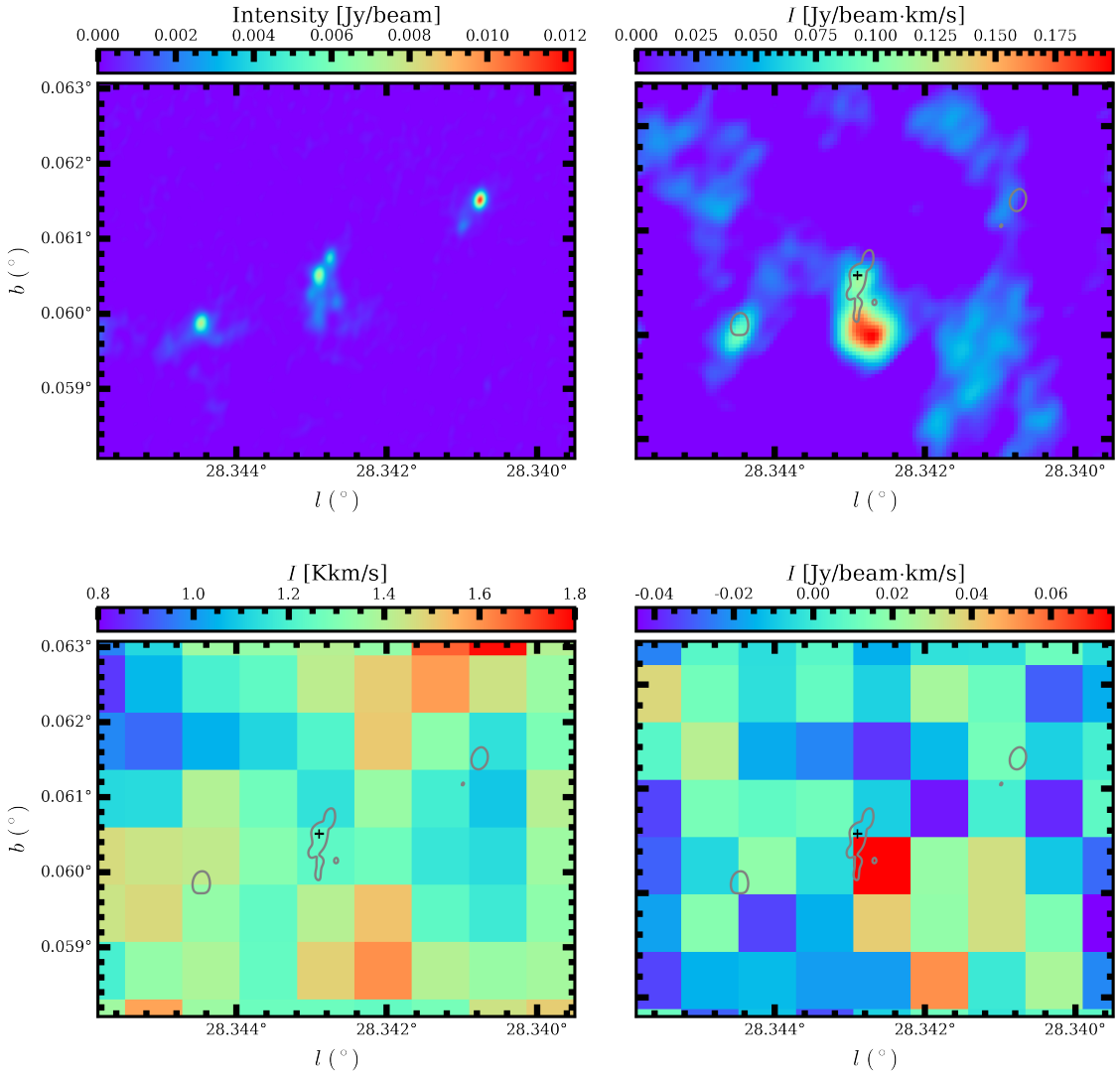

Figure A.1: As Figure 3.3, but for continuum peak 2, and with integration interval 77.5 – 78.5 km/s.

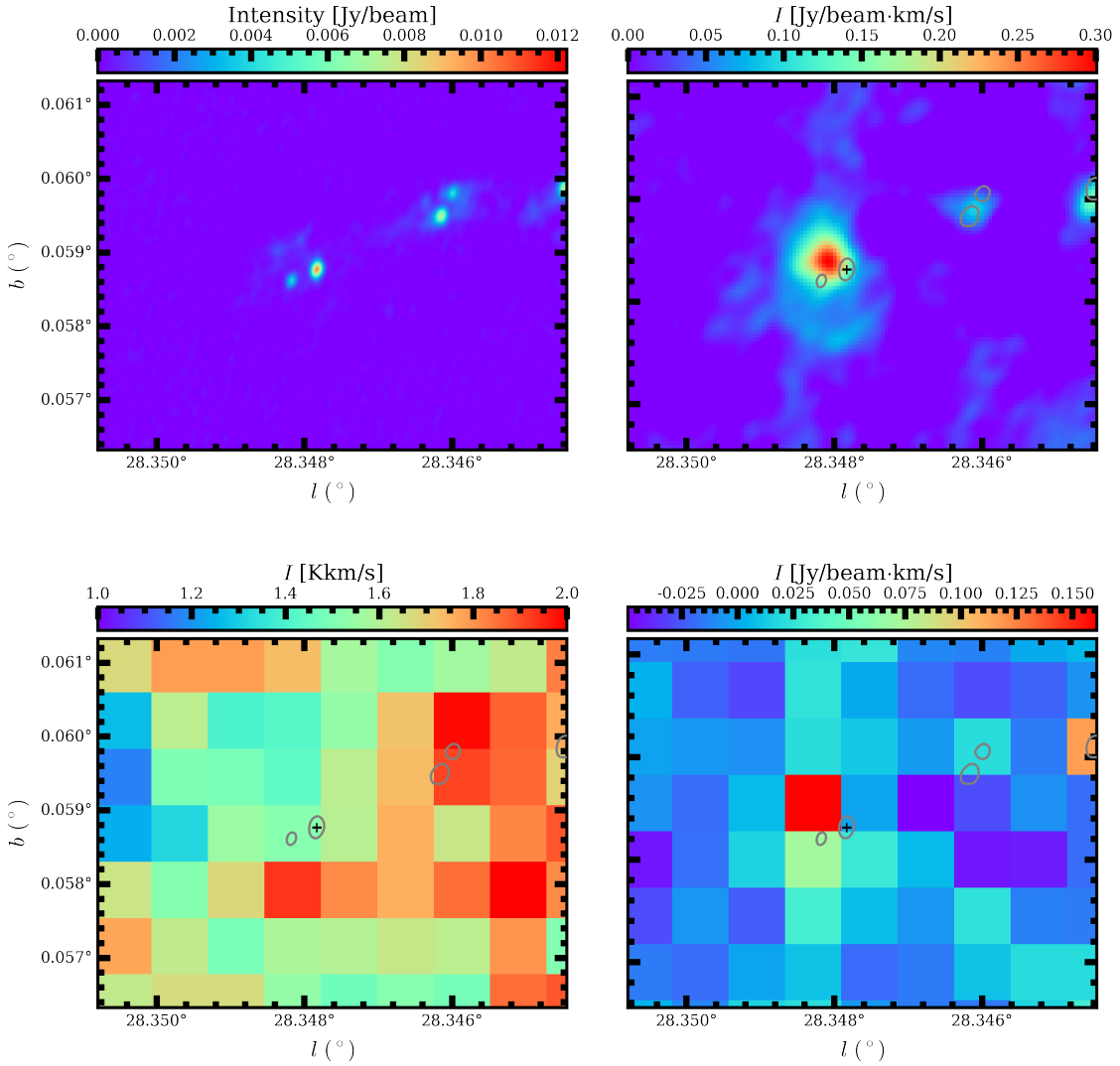

Figure A.2: As Figure 3.3, but for continuum peak 3, and with integration interval 77.5 – 78.9 km/s.

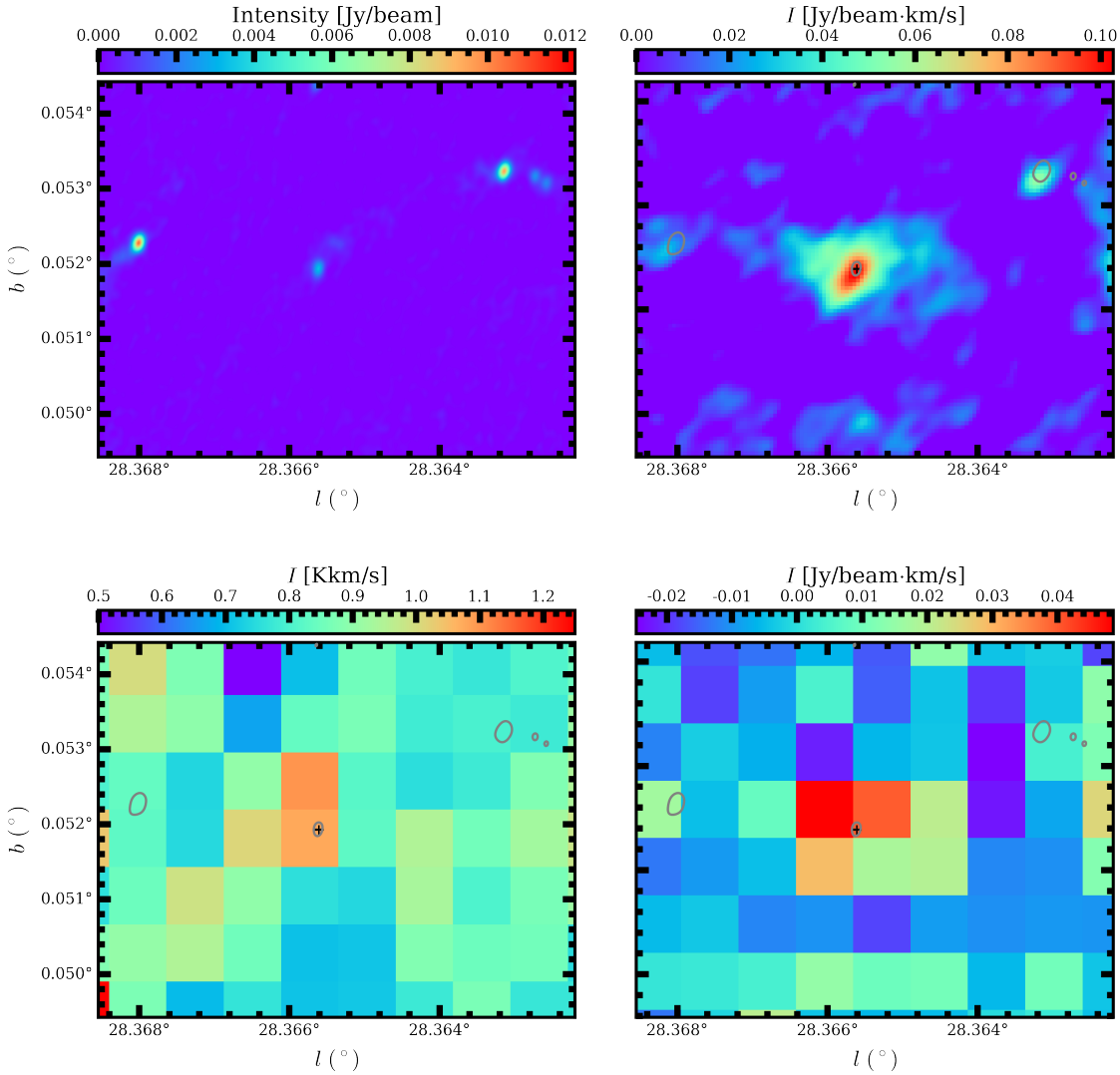

Figure A.3: As Figure 3.3, but for continuum peak 4, and with integration interval 78.6 – 79.2 km/s.

DEPARTMENT OF SOME SUBJECT OR TECHNOLOGY
CHALMERS UNIVERSITY OF TECHNOLOGY
Gothenburg, Sweden
www.chalmers.se

CHALMERS
UNIVERSITY OF TECHNOLOGY